Dissipation ratio and eddy diffusivity of turbulent and salt finger mixing derived from microstructure measurements

Jianing Li[1], Qingxuan Yang[1, 2, 3], Hui Sun[1]

[1]College of Oceanic and Atmospheric Sciences, Ocean University of China, Qingdao, China
[2]Physical Oceanography Laboratory/Institute for Advanced Ocean Study/Sanya Oceanographic Institution, Ocean University of China, Qingdao/Sanya, China
[3]Laboratory for Ocean Dynamics and Climate, Pilot National Laboratory for Marine Science and Technology, Qingdao, China

Correspondence to: Q. Yang (yangqx@ouc.edu.cn)

Abstract. Eddy diffusivity is usually estimated by using the Osborn relation assuming a constant dissipation ratio of 0.2. In this study, we examine dissipation ratios and eddy diffusivities of turbulent mixing and salt finger mixing based on microstructure datasets. We find the dissipation ratio of turbulence Γ^{T} is highly variable with a median value clearly greater than 0.2, which shows strong seasonal variation and decreases slightly with depth in the western equatorial Pacific, but obviously increases ~~in vertical~~with depth in the midlatitude Atlantic. Γ^{T} is jointly modulated by the Ozmidov scale to the Thorpe scale ratio R_{OT} and the buoyancy Reynolds number Re_b, namely $\Gamma^{\mathrm{T}} \propto R_{\mathrm{OT}}^{-4/3} \cdot Re_{\mathrm{b}}^{1/2}$. The eddy diffusivity based on observed Γ^{T} is larger than that estimated with 0.2, and presents a much stronger bottom enhancement. The eddy diffusivities of heat and salt for salt finger are calculated by two "analogical" Osborn equations; and their corresponding "effective" dissipation ratios $\Gamma_{\theta}^{\mathrm{F}}$ and Γ_{S}^{F} are explored. $\Gamma_{\theta}^{\mathrm{F}}$ scatters over two orders of magnitude with a median value of 0.47, and is mostly linearly correlated with Γ_{S}^{F} as $\Gamma_{S}^{\mathrm{F}} \approx 5\Gamma_{\theta}^{\mathrm{F}}$. The density flux ratio for salt finger decreases sharply with density ratio R_{ρ} smaller than 2.4 but regrows to a larger value with R_{ρ} exceeding 2.4. The salt finger-induced eddy diffusivities ~~become more~~also increase with depth, with some being comparable ~~or~~to even stronger than the mean turbulent ~~diffusivities with depth~~ones. This study highlights the influences of variable dissipation ratios and different mixing types on eddy diffusivity estimates, and should help ~~fur~~the~~r~~ improvement of mixing estimate and parameterization.

1 Introduction

Microscale turbulence in the ocean is patchy and intermittent. Compared with molecular diffusion, it mixes materials in a larger scale with a higher efficiency, playing a leading role in re-distributing heat (Pujiana et al., 2018), dissolved gases (Sabine et al., 2004), pollutants (Kukulka et al., 2016), nutrients and plankton (Whitt et al., 2017), thus shaping ocean general circulations and influencing bio-chemical processes in the ocean (Wunsch and Ferrari, 2004). These effects impact global environment and climate change (Jackson et al., 2008).

Due to these significant effects of microscale mixing, the outputs of ocean general circulation and climate models are deeply affected by the mixing intensity and variation (Jayne, 2009). Since the grid size is too coarse to resolve microscale processes, mixing parameterizations are mostly used as a proxy of turbulence effects in such models (Klymak and Legg, 2010). The proposing, verification and development of mixing parameterizations heavily rely on our perceptions of mixing intensity and spatiotemporal variation observed in the real ocean. Therefore, to accurately estimate eddy diffusivity based on observations has always been an unremitting pursuit of researchers. On one hand, many parameterization methods are developed and widely used to infer eddy diffusivity (e.g., GHP scaling, Gregg et al., 2003; MG scaling, MacKinnon and Gregg, 2003; and the Thorpe scale method, Dillon, 1982), thanks to abundant accumulation of traditional hydrographic observations. These methods yield a mediocre estimate based on fine-scale profiles of temperature and/or velocity with resolution significantly larger than microscale, and may have applicability problems induced by different mechanisms and hydrologic conditions (Mater et al., 2015). On the other hand, microstructure measurements provide a much more accurate estimate of turbulence behaviors (St. Laurent et al., 2012), although the amount of data is relatively small. With the development of observation technology and the advancement of instruments, microstructure data is experiencing a rapid growth. However, neither parameterizations nor microstructure measurements can directly provide eddy diffusivity values; what they infer is the dissipation rate of turbulent kinetic energy (TKE) ε. Assuming mixing is driven by turbulence, the eddy diffusivity of density is then estimated by the conventional Osborn relation, $K_\rho = \frac{R_f}{1-R_f} \cdot \frac{\varepsilon}{N^2}$ with $R_f/(1-R_f)=\Gamma^T=0.2$ (e.g., St. Laurent et al., 2012), where R_f is flux Richardson Number, N^2 is buoyancy frequency squared, and Γ^T is the dissipation ratio of turbulence.

However, there are two inadequacies in the application of the Osborn relation. First, the value of Γ^T should be carefully inspected. In the frame of steady, homogeneous turbulence, a balance between TKE production (P), buoyancy flux (B) and dissipation can be reached, $P+B-\varepsilon=0$. And Γ^T is the ratio of the buoyancy flux to the dissipation, B/ε, which describes the relative proportion of how much TKE is converted to potential energy and irreversibly dissipated to heat. Combining limited measurements with theoretical prediction, Osborn (1980) took the critical value of R_f as $R_f \leq 0.15$, resulting in $K_\rho < 0.2\varepsilon/N^2$. Following that, Γ^T is usually taken as a constant of 0.2. Eddy diffusivities of heat (K_θ), salt (K_S) and density are equal for turbulent mixing, so these diffusivity values can be easily determined by the Osborn relation as long as Γ^T is accurately measured. $\Gamma^T \approx 0.2$ is confirmed to be reasonable by some observations (Gregg et al., 2018); however, besides findings from laboratory experiments and direct numerical simulations (Barry et al., 2001; Jackson and Rehmann, 2003; Shih et al., 2005; Salehipour et al., 2016), there are considerable and accumulating observational evidence indicating Γ^T is significantly variable in both space and time, with a variation range covering several orders of magnitude, typically from 10^{-2} to 10^1 (Moum, 1996; Smyth et al., 2001; Mashayek et al., 2017; Ijichi and Hibiya, 2018; Monismith et al., 2018; Vladoiu et al., 2021; Li et al., 2023).

Observations conducted in different regions showed the statistical feature of Γ^T is significantly distinct from region to region, and the repeated measurements at some locations suggested Γ^T is obviously greater than 0.2 (Ijichi and Hibiya, 2018), indicating taking Γ^T=0.2 could significantly underestimate eddy diffusivity in these regions. Besides, microstructure measurements from both upper layer and the whole water column suggested Γ^T generally increases with depth, by as much as an order of magnitude (Ijichi and Hibiya, 2018; Li et al., 2023). Thus, taking Γ^T as a constant also leads to an underestimate of eddy diffusivity in the deep layer. These underestimated eddy diffusivities may be a part of the answer to "the missing mixing" puzzle (Wunsch and Ferrari, 2004). Some studies do show that the magnitude and pattern of Γ^T plays a key role in regulating global ocean general circulation (Mashayek et al., 2017; Cimoli et al., 2019). Moreover, Γ^T is reported to be modulated by turbulence features and is closely correlated with several parameters describing turbulence state, such as turbulence "age" R_{OT} (the ratio of the Ozmidov scale to the Thorpe scale; Ijichi and Hibiya, 2018) and turbulence "intensity" Re_b (buoyancy Reynolds number; Mashayek et al., 2017). However, different correlations between Γ^T and these parameters are found in different regions. Taking Re_b as an example, different studies concluded that their relation could be negatively correlated (Monismith et al., 2018), nonmonotonically correlated (Mashayek et al., 2017), or uncorrelated (Ijichi and Hibiya, 2018). In a word, taking Γ^T as a constant of 0.2 brings a large bias into eddy diffusivity estimate, yet our limited understanding prevents us from assigning a reasonable value for Γ^T.

The other inadequacy involves the driving mechanism of mixing. Although turbulent mixing dominates ocean mixing, there are considerable mixing events caused by the release of potential energy due to unstable temperature or salinity stratification (while the density stratification is stable), that is, double diffusion (Schmitt, 1994). Double diffusion has two manifestations, salt finger and diffusive convection. The former is associated with warmer, salter water overlying colder, fresher water; and the latter corresponds to the opposite scenario. Due to their unique requirements of vertical structures for temperature and salinity, diffusive convection is mostly prominent in the polar and subpolar regions, while salt finger prevails in the tropics and sub-tropical regions (van der Boog et al., 2021); and salt finger is our focus in this study. For the importance of salt finger mixing, analysis of global thermohaline staircase indicated salt finger only contributes a small fraction of the required energy to sustain mixing (van der Boog et al., 2021); however, not all salt finger events present staircases (St. Laurent and Schmitt, 1999), and the regional effects of salt finger mixing can be much profound (Fine et al., 2022). Some studies suggested salt finger mixing is significant when turbulent mixing is weak, while others suggested salt finger and turbulence can co-exist and interact with each other (Ashin et al., 2023). Unlike turbulent mixing, salt finger mixing, supplied by the release of potential energy, acts to strengthen the density stratification with a negative value of K_ρ. With P being negligible, the balance between B and ε leads to $R_f/(1\text{-}R_f)=-1$, and hence $K_\rho=-\varepsilon/N^2$ is applied to salt finger (McDougall, 1988). Therefore, if the mixing mechanism is not identified clearly, the conventional Osborn relation can estimate neither the correct sign nor the accurate magnitude of eddy diffusivity of density for salt finger mixing. Besides, the eddy diffusivities of heat, salt and density for salt finger mixing are inequivalent, namely $K_\theta<K_S$ (Schmitt et al., 2005). Therefore, K_θ and K_S for salt finger mixing cannot be estimated by the Osborn relation; and they can be calculated by a different manner involving the dissipation ratio Γ^F (note that Γ^F for salt finger is equivalent to $-K_\theta/K_\rho$ instead of $R_f/(1\text{-}R_f)$; St. Laurent and Schmitt, 1999), density ratio R_ρ (describing the relative contributions of temperature and salt to density) and density flux ratio r (the ratio of vertical heat flux to vertical salt flux) (see Section 2.3).

To overcome the shortcomings mentioned above, we turn to open microstructure datasets (Section 2), to first identify salt finger mixing from turbulent mixing (Section 3). Then, we explore the variability of Γ^{T} for turbulent mixing (Section 4.1), and examine Γ^{F} and the relation between R_ρ and r for salt finger mixing (Section 4.2). We also derive diffusivities K_ρ, K_θ and K_S and analyze them for both turbulent mixing and salt finger mixing (Section 5). A summary is given in Section 6.

2 Data and Methods

2.1 Data

We first thank the Climate Process Team for publicly sharing the "Microstructure Database" (MacKinnon et al., 2017). The data used in this study are selected from the shared microstructure sampling projects covering global oceans. Since the calculation of dissipation ratio requires the dissipation rate of thermal variance (χ_θ), and the vertical gradients of temperature θ and salinity S are needed, we chose all five projects that provide this variable. χ_θ and are in the form of vertical profiles. Besides χ_θ, θ and S, we also use ε, temperature θ and salinity S, which have all been standardized to the same vertical grid for each project. The locations, operating period, etc. of the five projects are given in Table 1 and Fig. 1. The MIXET projects are performed in the western equatorial Pacific, while the BBTRE and NATRE are conducted in the Atlantic between 40°S and 40°N. Salt finger is always active in the mid-to-low latitudes of the Atlantic, while its occurrence in the Pacific shows strong temporal variation (Oyabu et al., 2023). These data provide a great opportunity to investigate the spatial-temporal variation of dissipation ratio and eddy diffusivity induced by turbulent mixing and salt finger mixing.

Table 1. Information on the projects used in this study.

Project	Location	Period	Profile Number of Profiles	Vertical Resolution (m)
MIXET1	156°E, 0°-2°N	04.20-05.14, 2012	51	1
MIXET2	156°E, 0°-5°N	10.25-11.18, 2012	101	1
BBTRE96	10°-30°W, 12°-26°S	01.22-02.27, 1996	74	0.5
BBTRE97	15°-40°W, 10°-26°S	03.13-04.18, 1997	89	0.5
NATRE	20°-30°W, 24°-27°SN	03.25-04.22, 1992	150	0.5

MIXET: MIXing in the Equatorial Thermocline (Waterhouse et al., 2014; Richards et al., 2015)

BBTRE: Brazil Basin Tracer Release Experiment (Polzin et al., 1997)

NATRE: North Atlantic Tracer Release Experiment (St. Laurent and Schmitt, 1999; Polzin and Ferrari, 2004)

Formatted Table

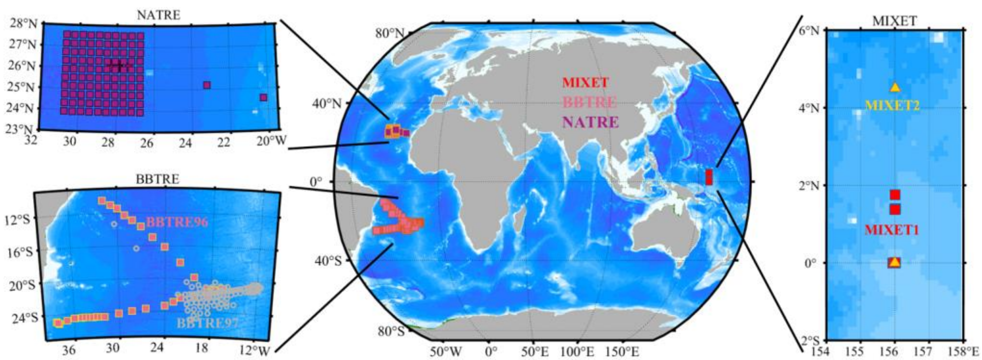

Figure 1: Station locations of the projects used in this study.

2.2 Identifying turbulent mixing and salt finger mixing

The profiles are divided into half-overlapped patches for further analysis. Following St. Laurent and Schmitt (1999), we choose 10 times of the vertical resolution as patch size, that is, 10 m (5 m) for projects with vertical resolution of about 1 m (0.5 m). We first examine if and which type of double diffusion is favorable for each patch in thermodynamical sense by the Turner angle, $Tu = \mathrm{atan}^{-1}(\alpha\theta_z - \beta S_z, -\alpha\theta_z + \beta S_z)$ (Ruddick, 1983). Here, α and β are the thermal expansion and saline contraction coefficients, respectively; θ_z and S_z are the vertical gradients of the original temperature and salinity profiles, respectively; and "atan^{-1}" is the four-quadrant inverse tangent. *Tu* varies between -180° and 180°, dividing water column into four thermodynamical regimes: doubly stable ($|Tu|<45°$), salt finger favorable ($45°<Tu<90°$), diffusive convection favorable ($-90°<Tu<-45°$), and gravitationally unstable ($|Tu|>90°$) (Ruddick 1983). *Tu* is related to density ratio R_ρ by $R_\rho=-\tan(Tu+45°)$. We exclude weak double diffusion signals ($45°<Tu<60°$ for salt finger favorable and $-60°<Tu<-45°$ for diffusive convection favorable) for further identification.

Formatted: Font: Italic

Besides the specific thermodynamical precondition, distinct statistical features are presented when double diffusion-induced mixing is dominant. First, Re_b is found to be no greater than $O(10)$ for active double diffusion (Inoue et al., 2007), and salt finger is rare for Re_b between 10 and 10^4 (St. Laurent and Schmitt, 1999). Re_b is defined as $\mathrm{Re}_b=\varepsilon/\nu N^2$, where ν is molecular viscosity coefficient. Moreover, double diffusion generally corresponds to elevated χ_θ (St. Laurent and Schmitt, 1999; Inoue et al., 2007), and the magnitude of χ_θ is significantly larger than ε when double diffusion prevails and turbulence is absent (Nagai et al., 2015). Therefore, we use $\mathrm{Re}_b<25$ and $|\chi_\theta|/|\varepsilon|\geq 7$ as additional criteria for the identification of double diffusion.

For doubly stable and gravitationally unstable water column, since their thermodynamical condition excludes the existence of double diffusion, we assume the mixing within the column is uniquely induced by turbulence only. The most prominent difference between turbulence patches with $|Tu|<45°$ and those with $|Tu|>90°$ is that Re_b of the former is significantly smaller than that of the latter. And $|Tu|$>90° generally means the presence of overturns. Therefore, the former patches are grouped as "weak turbulence", and the latter are "energetic turbulence".

Based on Tu, Re_b and $|\chi_\theta|/|\varepsilon|$, we classify the dominant mixing mechanisms into four types: weak turbulence ($|Tu|$<45° with small Re_b), energetic turbulence ($|Tu|$>90° with large Re_b), salt finger (60°<Tu<90°, Re_b<25 and $|\chi_\theta|/|\varepsilon|\geq 7$), and diffusive convection (-90°<Tu<-60°, Re_b<25 and $|\chi_\theta|/|\varepsilon|\geq 7$). Diffusive convection prevails mostly in the polar and subpolar regions (van der Boog et al., 2021); thus, it is rarely identified in this study (Section 3). As a result, diffusive convection is excluded from further analysis.

2.3 Estimating dissipation ratios and eddy diffusivities for turbulent mixing and salt finger mixing

Assuming steady and homogenous state, the production-dissipation balances for TKE (Osborn, 1980) and thermal variance (Osborn and Cox, 1972) are valid for both turbulence and salt finger (St. Laurent and Schmitt, 1999; Inoue et al., 2007),

$$(1 - R_f)K_\rho N^2 - R_f\varepsilon = 0, \qquad (1)$$

$$2K_\theta\theta_z^2 - \chi_\theta = 0. \qquad (2)$$

Define a general form of dissipation ratio Γ as $\frac{\chi_\theta N^2}{2\varepsilon\theta_z^2}$ (Oakey, 1985), combining (1) and (2) yields

$$\Gamma = \left(\frac{R_f}{1-R_f}\right)\frac{K_\theta}{K_\rho} = \left(\frac{R_f}{1-R_f}\right)\left(\frac{R_\rho-1}{R_\rho}\right)\left(\frac{r}{r-1}\right) = \frac{\chi_\theta N^2}{2\varepsilon\theta_z^2} \qquad (3)$$

where density flux ratio $r = \frac{\alpha K_\theta\theta_z}{\beta K_S S_z} = \frac{K_\theta}{K_S}\cdot R_\rho$.

For turbulent mixing, $\Gamma^T = R_f/(1-R_f)$; and the eddy diffusivities of heat, salinity and density for turbulent mixing are $K_\theta^T = K_S^T = K_\rho^T = \Gamma^T\frac{\varepsilon}{N^2}$. Here, we use superscripts "T" and "F" to indicate turbulent mixing and salt finger mixing, respectively.

For salt finger mixing, with $R_f/(1-R_f) = -1$, the eddy diffusivity of density can still be derived from the Osborn relation as $K_\rho^F = -\frac{\varepsilon}{N^2}$ (McDougall, 1988), which is five times of the conventional Osborn relation estimate and has a negative sign. However, the eddy diffusivities of heat and salinity for salt finger mixing are more complex (Schmitt et al., 2005),

$$K_\theta^F = \Gamma_\theta^F\frac{\varepsilon}{N^2} = \left(\frac{R_\rho-1}{R_\rho}\right)\left(\frac{r^F}{1-r^F}\right)\frac{\varepsilon}{N^2}, \qquad (4)$$

$$K_S^F = \Gamma_S^F\frac{\varepsilon}{N^2} = \frac{R_\rho-1}{1-r^F}\frac{\varepsilon}{N^2}. \qquad (5)$$

Note that (4) is actually $K_\theta^F = \chi_\theta/2\theta_z^2$, but in a form analogous to the Osborn relation. And these "analogical" Osborn relations for salt finger indicate the "effective" dissipation ratios for heat and salt are in different forms; but both are deeply related to the density flux ratio r^F and R_ρ. r^F can be derived as $R_\rho\frac{\chi_\theta N^2}{2\varepsilon\theta_z^2}/\left(R_\rho\frac{\chi_\theta N^2}{2\varepsilon\theta_z^2} + R_\rho - 1\right)$, and then used to infer K_θ^F and K_S^F.

Dissipation ratio Γ is defined as

$$\Gamma = \frac{\chi_\theta N^2}{2\varepsilon\theta_z^2} \qquad (1)$$

for turbulent mixing and salt-finger mixing (Oakey, 1985). Based on the production-dissipation balances for TKE and thermal variance (Osborn and Cox, 1972; Osborn,1980), and introducing R_ρ and the density flux ratio $r=\alpha K_\theta \theta_z/\beta K_S S_z=K_\theta/K_S \cdot R_\rho$, we get

$$\Gamma=\frac{\chi_T N^2}{2\varepsilon\theta_z^2}=\left(\frac{R_f}{1-R_f}\right)\frac{K_\theta}{K_\rho}=\left(\frac{R_f}{1-R_f}\right)\left(\frac{R_\rho-1}{R_\rho}\right)\left(\frac{r}{r-1}\right), \quad (2)$$

which is applicable to both turbulent mixing and salt finger mixing (St. Laurent and Schmitt, 1999).

For turbulent mixing only, $K_S=K_\theta=K_\rho$. Then, Eq. (2) leads to

$$\Gamma^{\mathrm{T}}=\frac{\chi_T N^2}{2\varepsilon\theta_z^2}=\frac{R_f}{1-R_f}, \quad (3)$$

and

$$K_\theta^{\mathrm{T}}=K_S^{\mathrm{T}}=K_\rho^{\mathrm{T}}=\Gamma^{\mathrm{T}}\frac{\varepsilon}{N^2}, \quad (4)$$

where superscript "T" indicates turbulent mixing.

However, for salt finger mixing only, with $\lim_{P\to 0}\frac{R_f}{1-R_f}=-1$ (St. Laurent and Schmitt, 1999), Eq. (2) yields

$$\Gamma^{\mathrm{F}}=\frac{\chi_T N^2}{2\varepsilon\theta_z^2}=-\frac{K_\theta}{K_\rho}=-\left(\frac{R_\rho-1}{R_\rho}\right)\left(\frac{r}{r-1}\right), \quad (5)$$

which cannot be used directly to estimate the salt finger induced eddy diffusivities. And they are estimated separately by introducing R_ρ and $r^{\mathrm{F}}=R_\rho\Gamma^{\mathrm{F}}/\left(R_\rho\Gamma^{\mathrm{F}}+R_\rho-1\right)$ (St. Laurent and Schmitt, 1999; Schmitt et al., 2005; Inoue et al., 2007),

$$K_\theta^{\mathrm{F}}=\left(\frac{R_\rho-1}{R_\rho}\right)\left(\frac{r}{1-r}\right)\frac{\varepsilon}{N^2}=\Gamma_\theta^{\mathrm{F}}\frac{\varepsilon}{N^2},\; K_S^{\mathrm{F}}=\frac{R_\rho-1}{1-r}\frac{\varepsilon}{N^2}=\Gamma_S^{\mathrm{F}}\frac{\varepsilon}{N^2}. \quad (6)$$

Note that all these equations are written into forms analogical to the Osborn relation for turbulent mixing. $\Gamma_\theta^{\mathrm{F}}$ and Γ_S^{F} are two artificial "mixing efficiencies", which are actually $\left(\frac{R_\rho-1}{R_\rho}\right)\left(\frac{r}{1-r}\right)$ and $\frac{R_\rho-1}{1-r}$ before "ε/N^2" for K_θ^{F} and K_S^{F} estimation. $\Gamma_\theta^{\mathrm{F}}$ is the same as Γ^{F}, while Γ_S^{F} are further derived based on R_ρ and r^{F}, $\Gamma_S^{\mathrm{F}}=\Gamma^{\mathrm{F}}\cdot R_\rho/r^{\mathrm{F}}$. Investigating the statistic features of $\Gamma_\theta^{\mathrm{F}}$ and Γ_S^{F} can be practically useful when estimating K_θ^{F} and K_S^{F} solely based on ε and N^2.

3 Statical features of turbulent mixing and salt finger mixing

Figure 2 suggests water properties vary greatly for the five projects, and Table 2 lists the proportions of patches for each mixing type. For the MIXET projects in the western equatorial Pacific, the *Tu* distribution in spring (MIXET1) shows a distinct shape from the autumn one (MIXET2). In spring, *Tu* shows double peaks at -30° and 110°, suggesting mixing is alternately dominated by weak and energetic turbulence, although the salt finger contribution accounts for 4.1% of the total patches and cannot be neglected. However, the autumn distribution is obviously unimodal, peaking at ~45°; and the dominant mixing types are first weak turbulence and secondly salt finger (~51.5% and 11.3%, respectively), with negligible energetic turbulence and diffusive convection. For the BBTRE projects, although they are conducted at different years, the operating seasons are similar: one in late-summer and the other early-autumn (Southern Hemisphere), so the seasonal variation cannot be studied. Their *Tu* distributions are similarly bimodal, with a leading peak at 70° and a weak one at -40°, suggesting the waters are mostly salt finger-favorable (although only about 5.9% is confirmed to be salt finger) and stable (33.3%), with rare energetic turbulence and neglectable diffusive convection-favorable contribution. For the NATRE, salt finger overwhelms the others, occupying more than 21% of the total patches; weak and energetic turbulence together hold 13.3%, with the diffusive convection favorable still being negligible (1%). ~~For these five projects, although almost half of the patches are salt finger favorable, only 9.7% of them shows~~For the BBTREs and NATRE, although a large proportion of the patches have 45°<*Tu*<90° and hence are salt finger favorable, most of them have elevated Re_b; thus, we infer these mixing events as hybrids of salt finger and turbulence but dominated by turbulence. These patches are excluded from analysis to highlight the difference between turbulent and salt finger mixing. Only a few patches are chosen as effective salt finger events. Therefore, as concluded in the following Section 5.3, it is turbulent mixing that dominates the observed microstructures, in line with the results based on the NATRE (St. Laurent and Schmitt, 1999). For these five projects, only 9.7% of patches show clear salt finger features. Weak turbulence has a higher percentage (32.0%), followed by 6.6% of energetic turbulence. Diffusive convection occurs less than 0.5% of the total patches, and is therefore negligible. Although dominated by turbulent mixing, the rest of the patches, more than 50%, are hybrids of different mixing types, and are excluded from the analysis.

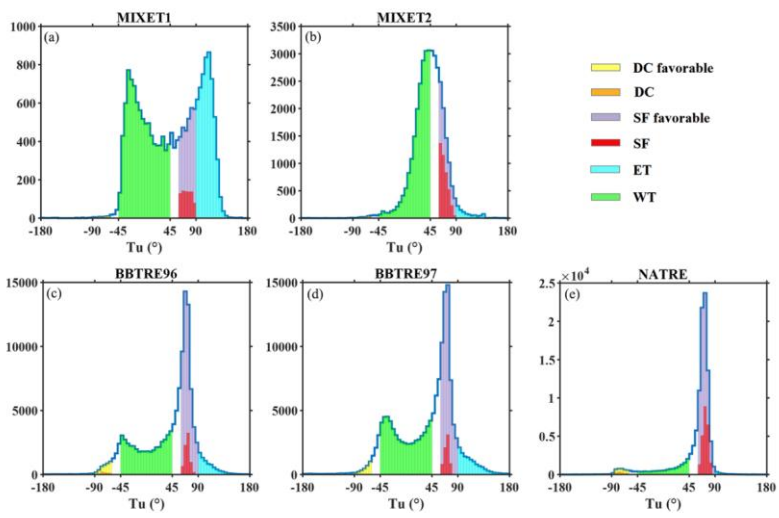

Figure 2: Histograms of patch-averaged *Tu* for different projects. Different *Tu* ranges of mixing types are marked by different colors: yellow for diffusive convection favorable (DC favorable; -90°<*Tu*<-60°), light purple for salt finger favorable (SF favorable;

60°<*Tu*<90°), cyan for energetic turbulence (ET), and green for weak turbulence (WT). The red and orange bars denote the actual ~~patch numbers~~number of patches of salt finger (SF) and diffusive convection (DC) selected by two more criteria, Re_b<25 and $|\chi_\theta|/|\varepsilon|\geq 5$, respectively.**

Table. 2. Proportions of patches with energetic turbulence, weak turbulence, salt finger, ~~and~~ diffusive convection and hybrid mixing types (turbulence and salt finger, or turbulence and diffusive convection) to the total ~~patch~~ number of patches for each project, and the sums for all the projects. Patches with hybrid mixing types are excluded from analysis.

	Proportion (%)				
	energetic turbulence	weak turbulence	salt finger	diffusive convection	excluded hybrid
MIXET1	29.56	47.05	4.11	0.06	19.22
MIXET2	2.48	51.48	11.32	0.16	34.56
BBTRE96	6.55	33.31	5.91	0.53	53.70
BBTRE97	8.67	38.19	4.56	0.08	48.50
NATRE	1.10	12.21	21.95	1.09	63.65
All	6.60	32.00	9.70	0.46	51.24

Inserted Cells

We compare the statistical differences of Re_b, ε, N^2, and χ_θ for energetic turbulence, weak turbulence and salt finger by considering all the patches from the five projects (Fig. 3). The salt finger patches are featured with the weakest turbulence intensity compared with weak and energetic turbulence patches, whose median Re_b are 5.0, 18.2 and 132.7, respectively. The median Re_b of energetic turbulence is slightly smaller than that reported in Mashayek et al. (2017) but close to the result of Ijichi and Hibiya (2018). Since the samples given here are from five different projects, their Re_b distributions are actually different: For MIXET projects, the median Re_b of energetic turbulence is small, only about 50; while the rest projects generally have a median Re_b around 200 for energetic turbulence. The variations of ε for different mixing types differ little, mostly ranging from 3×10^{-12} to 3×10^{-8} W kg^{-1}. Although the median ε for energetic turbulence is not obviously different from those for weak turbulence and salt finger (7.8×10^{-11}, 7.9×10^{-11} and 1.1×10^{-10} W kg^{-1}, respectively), it should be noted that most large ε values are induced by energetic turbulence. Distributions of χ_θ of weak turbulence and energetic turbulence differ little, but χ_θ of salt finger is clearly greater, in terms of variation ranges (salt finger: 3×10^{-11}-10^{-7} °C^2 s^{-1}; weak turbulence and energetic turbulence: 10^{-13}-10^{-7} °C^2 s^{-1}) and median values (salt finger: 1.8×10^{-9} °C^2 s^{-1}; energetic turbulence and weak turbulence: 1.5×10^{-11} °C^2 s^{-1}). Earlier studies considered the doubly stable regime as no mixing or excluded it from analysis (Inoue et al., 2007); however, besides some slight differences of proportion in large χ_θ and ε, energetic turbulence and weak turbulence share very similar distributions of χ_θ and ε (Figs. 3b, d), suggesting the doubly stable regime does not mean an absence of turbulence and should be dominated by weak turbulence. Stratification also presents different features for different mixing types. The energetic turbulence has the weakest stratification with a median of 6.1×10^{-7} s^{-2}, only 1/5 of that for weak turbulence. And salt finger presents the strongest stratification (1.9×10^{-5} s^{-2}). Clearly, the identified patches with energetic turbulence, weak turbulence and salt finger have distinct turbulent features, verifying the validity of the chosen criteria.

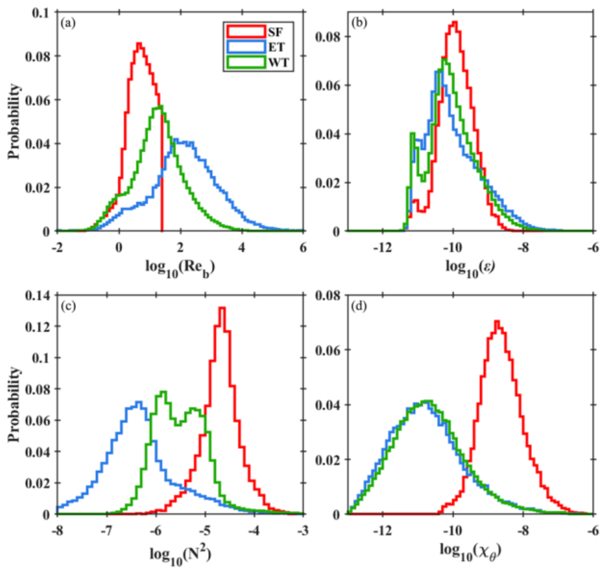

Figure 3: Probability-normalized histograms of $\log_{10}(Re_b)$ (a), $\log_{10}(\varepsilon)$ (b), $\log_{10}(N^2)$ (c), and $\log_{10}(\chi_\theta)$ (d) for different mixing types: SF (salt finger), ET (energetic turbulence) and WT (weak turbulence). Data of the five projects are taken as the whole collection.

A normalized occurrence frequency is calculated to quantify the vertical variation of each mixing type (Fig. 4). Taking energetic turbulence as an example, we first divide the number of energetic turbulence ~~patch number of~~ patches in each depth bin ~~to~~by the total number of energetic turbulence ~~patch number of~~patches in the whole project; then, to eliminate the vertical variation of observation frequency, we divide the results by the total ~~patch~~ number of patches within the same depth bin. This occurrence frequency is eventually normalized between 0 and 1 using its maximum. Consistent with some observations in the upper thermocline (Schmitt et al., 2005; van der Boog et al., 2021), salt finger is mostly prevailing in the upper 500-1000 m for all projects, with their occurrence frequencies reaching 1. For the MIXET projects and NATRE, the occurrence frequencies of salt finger gradually become weak and near zero with depth increasing to the seafloor. However, for the BBTRE projects, salt finger sharply disappears between 1000 and 2000 m and re-occurs at deeper depth (see Figure 10). The depth-colored T-S diagrams suggest the vertical transition of different water masses is responsible for the sudden disappearing of salt finger (Fig. 5). It is clear to see that both θ and S decrease with depth in most water columns, providing the basic precondition for salt finger. However, this tendency changes obviously between 1000 and 2000 m. At this depth range, θ changes little, but S increases drastically by at least 0.5; this prevents the occurrence of salt finger. This depth is just where the fresher Antarctic Intermediate Water transits to the North Atlantic Deep Water. Consequently, the occurrence frequency of salt finger is severely weakened at this depth. On the contrary to salt finger, energetic turbulence generally becomes more prevailing with increasing depth for most projects. The remarkably weak background stratification may contribute a lot to the flourish of energetic turbulence at depth, where even a weak perturbation can fully develop.

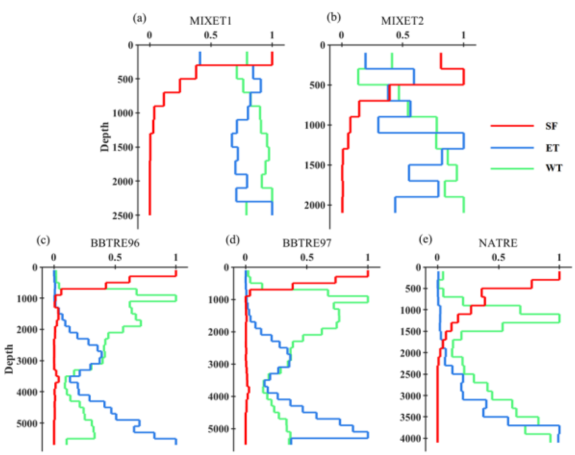

Fig. 4. Vertical variations of normalized occurrence frequency of salt finger (SF), energetic turbulence (ET) and weak turbulence (WT) for the five projects. The depth range is from 100 m to the deepest measurements, with a bin size of 200 m.

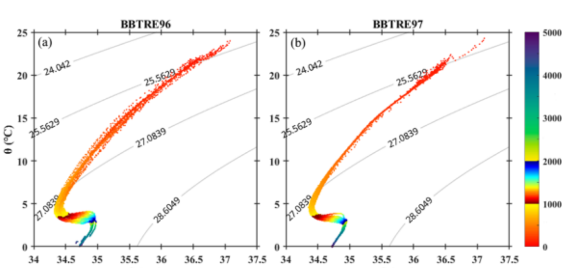

Fig. 5. T-S diagrams for BBTRE96 and BBTRE97. Color indicates patch depth, and the contour indicates isopycnic.

4 Γ variation of turbulence and salt finger

4.1 Γ variation of turbulence

Formatted: Heading 2

4.1.1 Vertical variation

We explore the variation of Γ^T first. Figure 6 suggests Γ^T varies in distinct manners for different projects. Results for the MIXET projects suggest Γ^T in the western equatorial Pacific is significantly seasonally variable. In spring (MIXET1), Γ^T of energetic turbulence varies between 2.5×10^{-2} and 1.7 (10^{th}-90^{th} percentiles) with a median of 0.23, smaller than that of weak turbulence ranging between 1.4×10^{-1} and 2.8 and peaking at 0.52. Γ^T in autumn is significantly elevated (MIXET2), and the medians and variation ranges for energetic turbulence and weak turbulence are [0.41 and from 3.4×10^{-2} to 8.8] and [0.58 and from 1.7×10^{-1} to 2.3], respectively. For the BBTRE projects, Γ^T of weak turbulence varies little between different years, with most patches varying between 10^{-2} and 10, although the median value in 1997 (0.35) was greater than that in 1996 (0.20). Γ^T of energetic turbulence is larger in 1997 than that in 1996, with median values of 0.48 and 0.20, respectively. Estimates from the NATRE also suggest Γ^T largely scatters between 10^{-2} and 10 for most patches; their median Γ^T values are 0.71 and 0.33 and 0.50 for energetic turbulence, and are 0.41 and 0.50 for weak turbulence, respectively. To summarize, besides the BBTRE and energetic turbulence of the MIXET projects showing a median value close to 0.2, the rest estimates are all clearly greater than 0.2. Γ^T for the five projects mostly vary within three orders of magnitude from 10^{-2} to 10, in line with other observations (Ijichi and Hibiya, 2018; Vladoiu et al., 2021; Li et al., 2023).

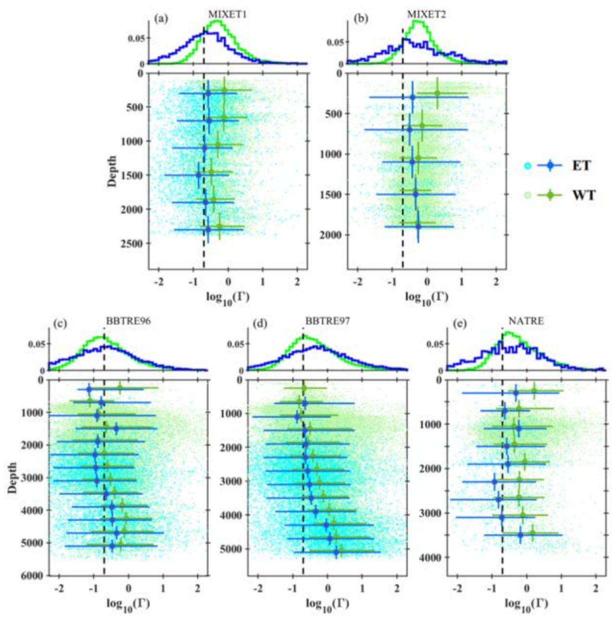

Fig. 6. Variations of Γ^T of energetic turbulence (ET) and weak turbulence (WT). Each panel consists of two sub-panels, with the upper one showing probability-normalized histogram of Γ^T, and the lower one being Γ^T-depth scatters; the median value of each depth bin is marked by a larger, darker dot overlying a cross marker, with horizontal bar indicating the 10th to 90th percentile range and vertical bar indicating the depth-bin range. The median Re_b values are compared between energetic turbulence and weak turbulence at each depth bin, and the median Γ^T corresponding to the larger Re_b is marked by a red dot. The conventional value of Γ^T, namely 0.2, is represented by the dashed black line.

For different projects, Γ^T varies with depth in different way. For the MIXET1, Γ^T of both energetic turbulence and weak turbulence fluctuate around their statistical median values weakly. For the MIXET2, the depth-median Γ^T of energetic turbulence varies between 0.2 and 0.7~~ alternately~~, with a slightly ~~increasing trend~~increase with depth. However, Γ^T of weak turbulence shows a clear decreasing from 2.5 at 300 m to 0.6 at 1400 m; then, it slightly increases to 0.8 at 1900 m. The Γ^T of weak turbulence for the BBTRE96 fluctuates around 0.2 in the upper 300 m, then it increases to ~1 at 4400 m and then decreases to ~0.6 at 5200 m. The scenario for energetic turbulence shares a similar picture. Γ^T of weak turbulence for the BBTRE97 departs little from 0.2 at depths above 1800 m, then monotonically increasing to ~2.3 at the deepest depth around 5200 m. Γ^T of energetic turbulence varies in a similar way in vertical, except the depth where trend~~s~~ change is 3000 m. For NATRE, Γ^T of energetic turbulence firstly decreases from 0.6 to 0.1 at 2300 m, then increases to 0.8 at 3500 m. As for weak turbulence, Γ^T stays around 0.8 between 600 and 3000 m and then increases beyond unity at 3500 m. In term of general trend by linear fitting Γ^T with depth, the five projects show two distinct vertical patterns of Γ^T: One is the ~~vertically~~ downward-decreasing pattern represented by the MIXET projects, and the other is the ~~vertically~~ downward-increasing one suggested by the rest projects over the midlatitude of the Atlantic. ~~Vertically~~Downward increasing Γ^T was also reported by Ijichi and Hibiya (2018). Their data collection sites spread over mid-to-high latitudes of the Pacific and Southern Ocean. Γ^T also presented a clear ~~vertically increasing trend~~downward increase in the upper 500 m of the South China Sea north of 10°N (Li et al., 2023). Combining all these observational results, we suggest Γ^T in the equatorial area should be treated differently, since it may decrease ~~in the vertical~~with depth, contrary to the ~~vertically increasing trend~~downward-increase away from the equator.

The full-depth statistics of the five projects disagree about ~~which~~whether Γ^T is larger for energetic turbulence ~~and~~or weak turbulence. However, when comparing Γ^T values of energetic turbulence and weak turbulence in the same depth bin, Γ^T of energetic turbulence is mostly smaller than that of weak turbulence. Considering that Re_b is reported to deeply modulate the variation of Γ^T (Mashayek et al., 2017; Monismith et al., 2018), and that energetic turbulence and weak turbulence have clearly different Re_b distributions (Fig. 3), we found energetic turbulence with smaller Γ^T generally has larger Re_b than weak turbulence, indicating a negative correlation between Γ^T and Re_b.

Formatted: English (United Kingdom)

Formatted: English (United Kingdom)

4.1.2 Relation between Γ^T, Re_b and R_{OT}

We then investigate the relations between Γ^T and Re_b for energetic turbulence and weak turbulence (Fig. 7). For the MIXET1, Γ^T of weak turbulence first decreases from 3.5 to 0.5 with Re_b increasing from 0.1 to 1, suggesting a relation of $\Gamma^T \propto Re_b^{-1}$, and then it weakly increases to 0.7 with Re_b reaching 100; and a weak decreasing in line with $\Gamma^T \propto Re_b^{-1/2}$ can be observed for $\mathrm{Re}_b>100$. For energetic turbulence, Γ^T generally decreases with Re_b, indicating $\Gamma^T \propto Re_b^{-1/2}$; this relation is consistent with the observations in the western Mediterranean Sea (Vladoiu et al., 2021). The pattern for the MIXET2 is similar to that for the MIXET1, although Γ^T of weak turbulence decreases in a smaller rate when Re_b is small and indicates $\Gamma^T \propto Re_b^{-1/2}$. Excluding the bins with few data points, Γ^T of weak turbulence for the BBTRE96 shows a weak ~~increasing trend~~increase from 0.2 to 0.3 as Re_b grows from 10 to 10^3 and a weak ~~decreasing trend~~decrease with Re_b exceeding 10^3. Γ^T and Re_b of weak turbulence for the BBTRE97 show similar relationships as those for the BBTRE96. The weak turbulence ~~trends~~variations for the BBTRE~~S~~s are the same as the estimates reported by Ijichi et al. (2020); and its shape is similar to the upper bound of the nonmonotonic $\Gamma^T \sim \mathrm{Re}_b$ relation proposed by Mashayek et al. (2017). It is notable that the scenario for energetic turbulence is distinct; Γ^T generally decreases from 5 to less than 0.1 with Re_b between 10 and 2.5×10^4 for the BBTRE96, forming a fitting slope steeper than -1/2 but flatter than -1. Γ^T of energetic turbulence for the BBTRE97 also shows a similar ~~decreasing trend~~decrease with Re_b. Except for the bins with few samples when $\mathrm{Re}_b<1$ and $\mathrm{Re}_b>10^4$, Γ^T of weak turbulence for the NATRE generally increases from 0.5 to 0.7, while Γ^T of energetic turbulence monotonically decreases from ~1 at $\mathrm{Re}_b=10^2$ to ~0.1 at $\mathrm{Re}_b=10^4$, suggesting $\Gamma^T \propto Re_b^{-1/2}$.

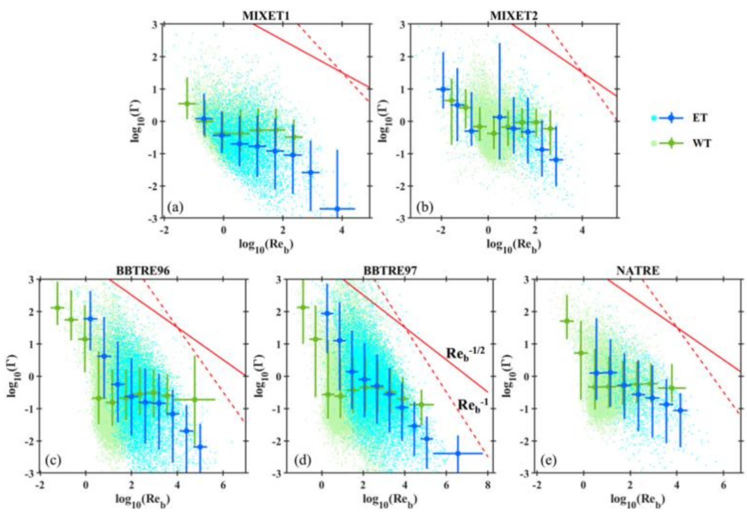

Fig. 7. Relations between Γ^T and Re_b for energetic turbulence (ET) and weak turbulence (WT). Overlying the light-color scatters of individual patches, Re_b -binned median values are marked by large darker dots; and the bin size and the 10th-90th percentile range of Γ^T are denoted by the horizontal and vertical bars, respectively. The solid and dashed red lines mark $\Gamma^T \propto Re_b^{-1/2}$ and $\Gamma^T \propto Re_b^{-1}$, respectively.

Although Γ^T generally decreases with Re_b in most cases of the five projects, the decreasing rate varies with projects and Re_b ranges. There are several cases showing Γ^T stays constant or even increases with Re_b. These suggest Γ^T is not solely modulated by Re_b; and there may be other factors that influence Γ^T in a comparable or even dominating role relative to Re_b. R_{OT} is reported as such a parameter that regulates Γ^T more strongly than Re_b, $\Gamma^T \propto R_{OT}^{-4/3}$ (Ijichi and Hibiya, 2018). R_{OT} is the ratio of the Ozmidov scale L_O to the Thorpe scale L_T, $R_{OT}=L_O/L_T$ with $L_O=\varepsilon^{1/2}/N^{3/2}$ and $L_T = \langle \delta_T^2 \rangle^{\frac{1}{2}}$, where the Thorpe displacement δ_T is the depth difference of a water parcel between the original and sorted potential temperature profiles of an overturn. Overturns are identified by the cumulative Thorpe displacement $\sum \delta_T$ (Mater et al., 2015; Ijichi and Hibiya, 2018). Because the vertical resolution of temperature profiles is 1 m or 0.5 m, overturns with vertical size of $O(1)$ m or smaller cannot be identified. Additionally, the identified overturns with size smaller than 10 m or greater than 400 m are excluded from analysis, because the former contain too few data points and the latter are possibly the vertical structures of different water masses instead of genuine turbulent overturns. We also estimate the overturn-averaged Tu, Γ^T and Re_b. Due to the coarse vertical resolution of temperature profiles used in our study, only a few overturns meet the identification criteria for each project; as a result, the overturns of the five projects are taken as one collection (total ~~overturn~~ number of overturns is 3862).

Figure 8 shows the overturn-based relation between Γ^T and R_{OT}. Since most overturns are identified at depth, with only one fifth shallower than 1000 m but more than one third at depth below 2000 m, the overturn-based Γ^T is clearly greater than 0.2, with a median value of 0.91. In Fig. 8, although overturns are evenly scattered in the R_{OT}-Γ^T space, the probability density shows they concentrate around two sites mostly, one with R_{OT} and Γ^T of (0.03, 1.19) and the other (0.56, 0.53). These two clusters are well distinguished by Re_b, with the first location corresponding to Re_b<160 (median value is 25) and the other to Re_b>160 (median value is 835). For both clusters, the contours of probability density tilt at slopes of -4/3, confirming $\Gamma^T \propto R_{OT}^{-4/3}$ is valid for each cluster. However, the general trend between R_{OT} and Γ^T for the whole data collection is much flatter, with a slope of only about -1/2. Comparing Re_b of the two clusters, it is easy to find that Re_b grows exponentially with R_{OT}. Therefore, the general variation of Γ^T with the growth of R_{OT} is not only influenced by R_{OT}, but also partly affected by Re_b. Supposing Γ^T is mostly modulated by these two parameters, and considering the decrease ~~trend~~ of Γ^T with R_{OT} is significantly weakened by Re_b, this suggests a ~~positively~~positive relation between Γ^T and Re_b.

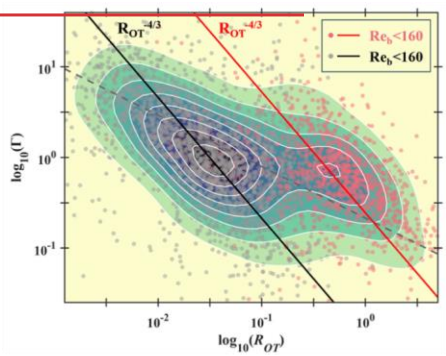

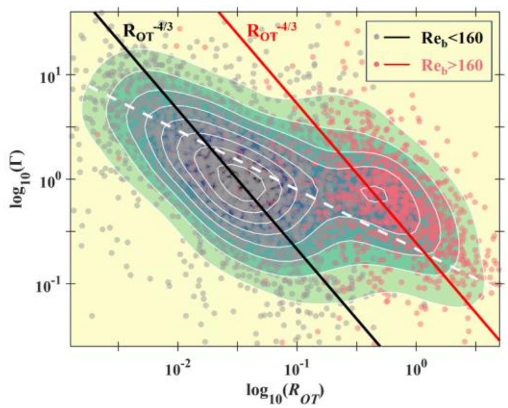

Fig. 8. Relation between overturn-based Γ^T and R_{OT}, overturns from the five projects are considered. The shading describes the distribution of probability density, with yellow indicating minimum probability density and blue representing maximum one. The overturns are correspondingly divided into two clusters: the gray dots have $Re_b<160$, and the pink ones, $Re_b>160$. The black and red lines represent $\Gamma^T \propto R_{OT}^{-4/3}$, crossing the centers of the two clusters. The ~~gray~~white dashed line is the general relation between Γ^T and R_{OT} of the whole data collection.

Formatted: Font: (Default) Cambria Math

Figure 9 shows the variation of median value of Γ^T jointly binned by Re_b and R_{OT}. Note that most parts of the Re_b-R_{OT} space are null, with all the data gathered around a band originating from large Re_b and R_{OT} to small Re_b and R_{OT}. This confirms that Re_b and R_{OT} are positively correlated in general. As for the median Γ^T, although its value is scattered, its general pattern indicates Γ^T grows fastest along a direction from small Re_b and large R_{OT} to large Re_b and small R_{OT}, suggesting that Γ^T is indeed positively correlated with Re_b and negatively correlated with R_{OT}. Assuming $\Gamma^T \propto R_{OT}^{-4/3} \cdot Re_b^{c}$, we substitute the median values of Γ^T, Re_b and R_{OT} in Fig. 9 into this relation to fit the exponent c. The fitting results suggest $c \approx 1/2$ and a relation of $\Gamma^T \approx 10^{-3} \cdot R_{OT}^{-4/3} \cdot Re_b^{1/2}$. The isolines of this relation are shown in Fig. 9, which can well capture the main variation ~~trend~~ of Γ^T with Re_b and R_{OT}. Based on the microstructure measurements collected from the upper layer in the South China Sea, Li et al. (2023) presented a relation of $\Gamma^T \approx aR_{OT}^{-4/3} \cdot Re_b^{1/2}$, but a is around 0.02 in that region, one magnitude larger than the value presented here. This is because Re_b have much smaller magnitude in the upper South China Sea, with most Re_b varying between 10^{-1} and 10^3. Therefore, compared with the results in Li et al. (2023), the larger Re_b in this study lead to a relatively smaller a. On the other hand, the significant variation of a may suggest some other parameters can influence Γ^T besides Re_b and R_{OT}.

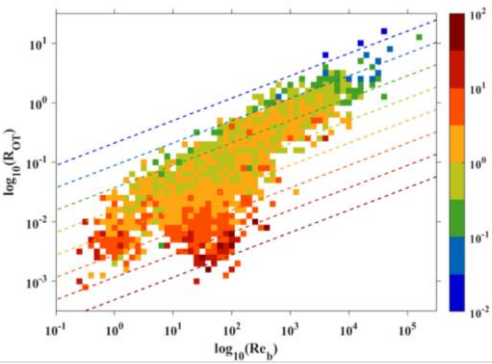

Fig. 9. Variation of median Γ^T binned by R_{OT} and Re_b, based on overturn estimates of the five projects. ~~The~~The color bar refers to the median Γ^T, and the colored dashed lines indicate the isolines of $10^{-3}\cdot R_{OT}^{-4/3}\cdot Re_b^{1/2}$.

4.2 Γ variation of salt finger

Γ^F has been widely used to distinguish salt finger from turbulence, since its value is reported to be larger than the conventional Γ^T value of 0.2 (St. Laurent and Schmitt, 1999). However, the full-depth observations presented in either this study or previous ones indicate 0.2 is an underestimate of Γ^T, the difference of dissipation ratio between turbulent mixing and salt finger mixing in the deep water needs to be examined. Figure 10 presents the variations of Γ_θ^F and Γ_S^F with depth. Compared with Γ^T varying over three orders of magnitude, both Γ_θ^F and Γ_S^F are less variable and change by two orders in magnitude or as small as one order. The median Γ_θ^F for all samples from the five projects is 0.47, slightly smaller than the Γ^F observed in the diurnal thermocline of the Arabian Sea (0.65; Ashin et al., 2023), in the Kuroshio Extension Front (~1; Nagai et al., 2015), and in the thermocline of the western tropical Atlantic (~1.2; Schmitt et al., 2005). The median Γ_θ^F for the five projects are distinct: 0.25, 0.29 and 0.28 for the MIXET1, BBTRE96 and BBTRE97, similar to the conventional Γ^T value of 0.2; 0.52 for NATRE, distinguishable from 0.2 but close to their observed Γ^T (Fig. 6); 0.98 for the MIXET2, significantly larger than 0.2 and different from their observed Γ^T (Fig. 6). This suggests the dissipation ratio difference between turbulence and salt finger is complex.

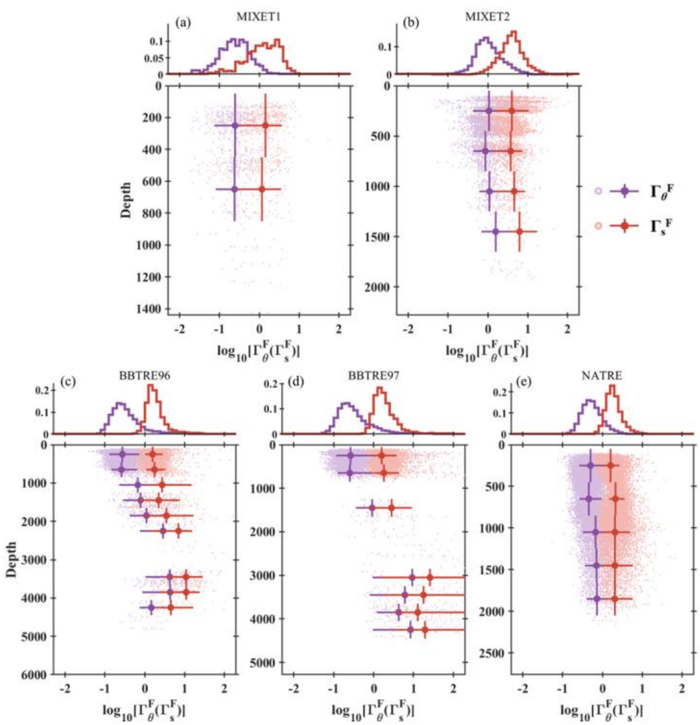

Fig. 10. Variations of $\Gamma_\theta^F(\Gamma_S^F)$ of salt finger for the five projects. Each panel consists of two sub-panels, with the upper one showing the probability-normalized histograms of Γ_θ^F and Γ_S^F, and the lower one being their vertical variations. The median value of each depth bin is marked by a larger, darker dot overlying a cross marker, with horizontal bar indicating the 10th to 90th percentile range and vertical bar indicating the depth-bin range.

Vertically, Γ_θ^F for MIXET1 keeps nearly constant as 0.25. While Γ_θ^F for MIXET2 first decreases from 1 to 0.7 in the upper 700 m and then slightly increases to 2 at 1500 m. Γ_θ^F present a similar vertical trend for both BBTRE96 and BBTRE97: Γ_θ^F is small and stays as a constant within the upper 800 m, with a median of 0.28; with depth increasing to 3000 m, it significantly increases over orders of magnitude, and the median value reaching ~10; it is weakened at deeper depth. Note that the relatively small median Γ_θ^F for the BBTRE projects is mainly caused by the dominant patches with small Γ_θ^F values in the upper 800 m; and Γ_θ^F at depth is actually very large and significantly greater than 0.2 or the observed Γ^T. The scenario for the NATRE is similar to that for the MIXET2, whose depth-median Γ_θ^F remains nearly consistent around ~0.5, although a very weak ~~increasing~~positive trend exists.

The “effective” salt dissipation ratio Γ_S^{F} tends to be obviously larger than $\Gamma_\theta^{\mathrm{F}}$ (Fig. 10). With the overall median Γ_S^{F} of 1.87, the median values of Γ_S^{F} for the five projects are 1.35 (MIXET1), 3.98 (MIXET2), 1.67 (BBTRE96), 1.71 (BBTRE97), and 1.83 (NATRE), floating around the value reported in the thermocline of the western tropical Atlantic of ~2.8 (~~ref).~~Schmitt et al., 2005). Γ_S^{F} is strongly positively proportional to $\Gamma_\theta^{\mathrm{F}}$, with the median values of $\Gamma_S^{\mathrm{F}}/\Gamma_\theta^{\mathrm{F}}$ for the five projects being 5.1, 3.7, 6.3, 6.9, and 3.8, respectively. Thus, a general relation of $\Gamma_S^{\mathrm{F}}\approx 5\Gamma_\theta^{\mathrm{F}}$ can be inferred. Due to this correlation, Γ_S^{F} presents vary similar vertical variation as $\Gamma_\theta^{\mathrm{F}}$.

Note that $\Gamma_S^{\mathrm{F}}/\Gamma_\theta^{\mathrm{F}}$ is equivalent to R_ρ/r^{F}~~.~~ (Eq. (6)). Since R_ρ is relatively easy to calculate, as a result, it is an alternate way to infer the hard-to-measure r^{F}. R_ρ and r^{F} are the key parameters to estimate the dissipation ratios of heat and salt for salt finger (Section 2.3). Therefore, many studies tried to explore the relation of R_ρ and r^{F} based on theoretical derivations, laboratory experiments and numerical simulations (Kelley, 1986; Kunze, 1987; Radko and Smith, 2012). Here, the R_ρ-r^{F} diagram colored by probability density for the five projects indicate the salt finger patches are rather scattered (Fig. 11). However, the median r^{F} binned by R_ρ shows a clear nonmonotonic variability. For R_ρ increasing from 1 to 2.4, r^{F} decreases from ~0.8 to 0.4; then, it gradually increases to 0.55 with R_ρ approaching 3.7. This correlation between R_ρ and r^{F} can be well fitted by

$$r^{\mathrm{F}} = \frac{0.79\cdot R_\rho^2 - 2.96\cdot R_\rho + 3.18}{R_\rho^2 - 3.26\cdot R_\rho + 3.46}$$ ~~(6~~ (7)

Compared with other correlation curves (Kelley, 1986; Kunze, 1987; Radko and Smith, 2012), all of them present a r^{F} ~~decreasing trend~~decrease for R_ρ smaller than 2, although the variation range and rate differ. The most obvious discrepancy between them is that r^{F} tends to regain a larger value with R_ρ exceeding 2.4 in our study, while all the other curves decrease little to asymptote to a constant value. The observational result presented here falls in the area outlined by the existing results. For our results, the salt finger patches with R_ρ<2.5 are abundant and mostly concentrated to indicate a negative correlation between R_ρ and r^{F}. It needs to be mentioned that patches with R_ρ>2.5 are much rare and sparsely distributed, making the ~~increasing trend~~increase of r^{F} in larger R_ρ range need to be treated carefully.

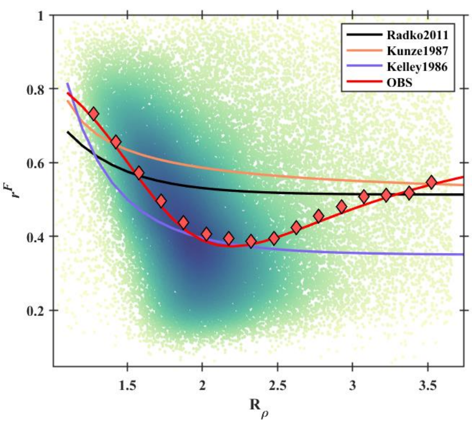

Fig. 11. Relation between R_ρ and r^F. Salt finger patches from all the five projects are considered. Dots are colored by probability density, with darker color indicating larger probability density. The median r^F binned by R_ρ are marked by red diamonds with black edge, and the red curve is the fitting curve. The black, orange and purple curves are adopted from Radko and Smith (2011), Kunze (1987) and Kelley (1986), respectively.

We also investigate the relation between observed Γ_θ^F and Re_b (Fig. 12), which differs considerably between different projects. For the MIXET1, a nearly linear decreasing trenddecrease of Γ_θ^F (in logarithmic scale) from ~1 to ~0.1 can be easily observed for all patches with Re_b between 0.3 and 25, indicating $\Gamma_\theta^F \propto Re_b^{-1/2}$. Γ_θ^F for MIXET2 with Re_b<2.5 are also well fitted as $\Gamma_\theta^F \propto Re_b^{-1/2}$, but Γ_θ^F for Re_b>2.5 tends to remain a constant of 0.7. For the BBTRE projects, when Re_b<3, Γ_θ^F decreases at a larger rate than the MIXET projects, $\Gamma_\theta^F \propto Re_b^{-1}$, and Γ_θ^F stays almost unchanged when Re_b exceeds 3. Γ_θ^F for the NATRE stays as a constant of 0.7 with most Re_b ranging from 1 to 25. Due to the strong correlation between Γ_S^F and Γ_θ^F, the dependence of Γ_S^F on Re_b is similar to that of Γ_θ^F, although variation rates are different for some projects. Taking all the projects together, Γ_θ^F and Γ_S^F decrease with Re_b in general; however, the decreasing rate of decrease varies greatly with projects and different Re_b bands, indicating Γ_θ^F and Γ_S^F may also be modulated by variables other than Re_b.

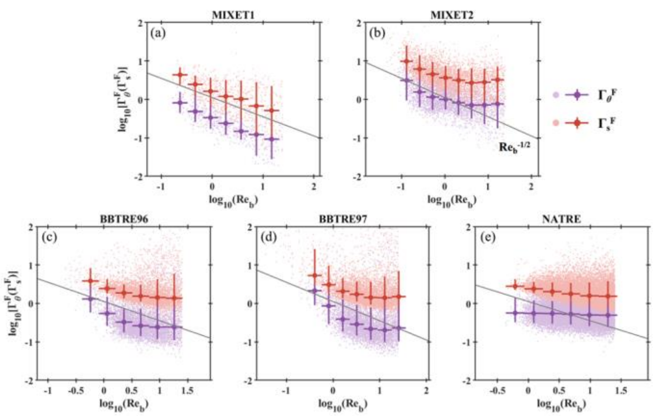

Fig. 12. Relations between $\Gamma_\theta^F(\Gamma_S^F)$ and Re_b for the five projects. Overlying the light-color scatters of individual patches, the Re_b-binned median values are marked by darker large dots. The bin size and 10th-90th percentile range are denoted by the horizontal and vertical bars, respectively. The gray line in each panel marks $\Gamma_\theta^F(\Gamma_S^F) \propto Re_b^{-1/2}$.

Formatted: Font: Cambria Math

5 Eddy diffusivities induced by turbulence and salt finger

5.1 Eddy diffusivities induced by turbulence

Since Γ^T deviates from the conventionally used constant of 0.2 in the Osborn relation, K_ρ^T (also K_θ^T and K_S^T) based on Γ^T differs from K_c based on 0.2 (K_c=0.2ε/N^2) to different extents (Fig. 13). For the MIXET1, since Γ^T is only slightly larger than 0.2 in general, the magnitudes of K_ρ^T and K_c differ slightly, with mean K_c =2.1×10^{-6} m^2 s^{-1} and mean K_ρ^T =4.6×10^{-6} m^2 s^{-1}. Vertically, both K_ρ^T and K_c decrease in the upper 1200 m and increase at deeper depth. Obvious differences between K_ρ^T and K_c occur at depth ranges shallower than 1200 m and deeper than 2000 m, where the mean ratio of K_ρ^T to K_c are 2.7 and 2.3, respectively. For the MIXET2, the magnitude difference between K_ρ^T and K_c is larger, with the mean values being 1.3×10^{-6} m^2 s^{-1} and 3.9×10^{-6} m^2 s^{-1}, respectively. Compared with K_c that stays nearly constant in the upper 1700 m, K_ρ^T first decreases in the upper 700 m and then stays around 2×10^{-6} m^2 s^{-1} between 700 and 1700 m. For the BBTRE96, except for several depth bins, the difference between mean K_ρ^T and mean K_c in the upper 3700 m is small; and they share similar ~~vertical increasing rates~~downward increases and similar depth-averaged median values around 2.0×10^{-5} m^2 s^{-1}, with K_ρ^T is about 2.5 times of K_c. Although both increase at depths deeper than 3700 m, K_ρ^T is nearly 4.7 times larger than K_c; and the mean values for K_ρ^T and K_c are 5.0×10^{-4} and 1.1×10^{-4} m^2 s^{-1}, respectively. For the BBTRE97, K_ρ^T and K_c share the same ~~vertical decreasing~~downward negative trend and magnitude in the upper 1000 m, with mean values close to 2.6×10^{-5} m^2 s^{-1}. Beneath 1000 m, although sharing similar ~~increasing~~positive trend, K_ρ^T becomes larger and larger than K_c with depth. At depth between 1000 and 3700 m, $K_\rho^T/K_c \approx 2.7$ with median K_ρ^T around 8.3×10^{-5} m^2 s^{-1}, while the corresponding values for depths deeper than 3700 m are $K_\rho^T/K_c \approx 8.8$ and mean $K_\rho^T \approx 1.2\times10^{-3}$ m^2 s^{-1}. For the NATRE, K_ρ^T is always larger than K_c at all depth ranges; and the mean values of K_ρ^T and K_c are 4.4×10^{-5} and 1.0×10^{-5} m^2 s^{-1}, respectively. Vertically, K_c generally fluctuating around its mean value for the whole water column. K_ρ^T also shows no clear vertical ~~trend~~variation in the upper 2700 m, but it increases significantly from 2.6×10^{-5} m^2 s^{-1} at 2700 m to 1.2×10^{-4} m^2 s^{-1} at 3900 m. As a result, K_ρ^T is 13.7 times larger than K_c at 3900 m. For the five projects, taking Γ^T as a constant of 0.2 underestimates the actual eddy diffusivity induced by turbulence, and this underestimate may become more severe as Γ^T increases with depth.

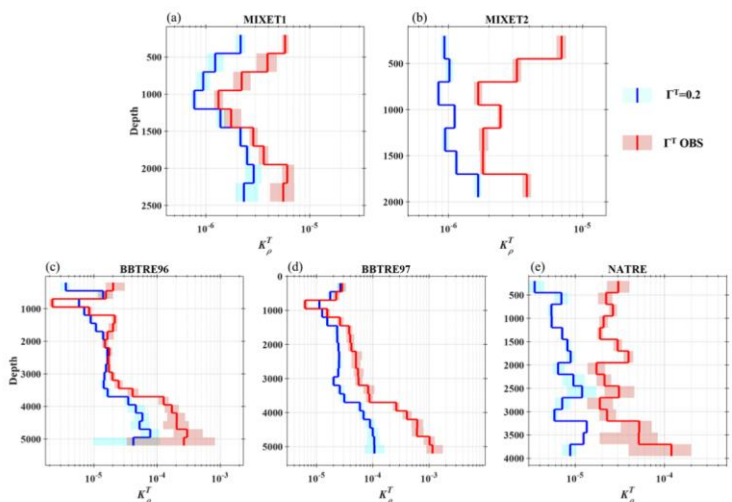

Fig. 13. Vertical profiles of depth-bin mean $K_\rho^T(K_c)$ based on energetic turbulence and weak turbulence patches for the five projects. The blue curve is K_c estimates by using Γ^T=0.2, and the red curve is K_ρ^T based on the measured Γ^T. The colored shadings correspond to 95% bootstrapped confidence intervals. To exclude the influence of extreme values, we only consider patches with Γ^T ~~within~~between its upper and lower quartiles for each depth bin. The depth-bin size is 250 m.

5.2 Eddy diffusivities induced by salt finger

For salt finger-induced eddy diffusivities, some studies estimated their values by taking a constant r^F around 0.7 (0.75 in Schmitt et al., 2005; 0.6 in St. Laurent and Schmitt 1999). Here, K_θ^F derived from the observed r^F is compared with the r^F=0.7 estimate, $K_\theta^F{}_c$ (Fig. 14). Depending on the deviation of the observed r^F from 0.7, the five projects are distinct in terms of the difference between K_θ^F and $K_\theta^F{}_c$. For the MIXET1, K_θ^F and $K_\theta^F{}_c$ both vary little with depth. But the magnitude of $K_\theta^F{}_c$ is significantly greater than that of K_θ^F, with mean values being 2.2×10^{-6} and 4.6×10^{-7} m^2 s^{-1}, respectively. This is in line with the fact that the mean value of the measured r^F for the MIXET1 is only 0.37, about one half of 0.7. For MIXET2, with the median r^F elevated to 0.63, $K_\theta{}^F{}_c$ is only slightly larger than $K_\theta{}^F$. And they both increase with depth form $O(10^{-6})$ m^2 s^{-1} at 100 m to $O(10^{-5})$ m^2 s^{-1} at 1850 m. The median values of $K_\theta{}^F{}_c$ and $K_\theta{}^F$ are 4.4×10^{-6} m^2 s^{-1} and 3.2×10^{-6} m^2 s^{-1}, respectively. The difference between MIXET1 and MIXET2 indicates a strong seasonal variation of salt finger in the tropical Pacific. For both BBTRE96 and BBTRE97, $K_\theta{}^F{}_c$ is significantly larger than $K_\theta{}^F$ in the upper layer with magnitudes around $O(10^{-5})$ and $O(10^{-6})$ m^2 s^{-1}, respectively, and this difference turns small as they both increase to 2×10^{-5} m^2 s^{-1} with depth increasing to 2000 m. At deeper depths, although salt finger disappears at some depth ranges, $K_\theta{}^F{}_c$ varies little around 2.5×10^{-5} m^2 s^{-1}. $K_\theta{}^F$ is generally larger than $K_\theta{}^F{}_c$ between 2400 m and 3400 m with $K_\theta{}^F/K_\theta{}^F{}_c$ varying between 3 and 10, and this ratio drops to less than 2 for depths deeper than 3400 m. For NATRE, both $K_\theta{}^F$ and $K_\theta{}^F{}_c$ present clear vertical increasing trendsdownward increases, and $K_\theta{}^F{}_c$ is dominantly greater than $K_\theta{}^F$. The difference between $K_\theta{}^F$ and $K_\theta{}^F{}_c$ is reduced with increasing depth, due to the fact that $K_\theta{}^F$ increases much faster in the verticalwith depth from about 2×10^{-6} m^2 s^{-1} at upper 500 m to 1.5×10^{-5} m^2 s^{-1} at 2400 m. For all the projects, $K_\theta{}^F$ is generally smaller than $K_\theta{}^F{}_c$ since r^F is mostly smaller than 0.7; and this phenomenon is most obvious in the upper layer (upper 1000 m of the BBTRE96, BBTRE97, and NATRE). At deeper depths, $K_\theta{}^F>K_\theta{}^F{}_c$ can be observed in projects like the BBTRE96, BBTRE97. All these indicate r^F is highly variable regionally and vertically. We also explore vertical variation of $K_S{}^F$, which is very similar to that of $K_\theta{}^F$ but with a larger magnitude (Fig. 15), as the result of $\Gamma_S{}^F$ being larger than and strongly proportional to $\Gamma_\theta{}^F$.

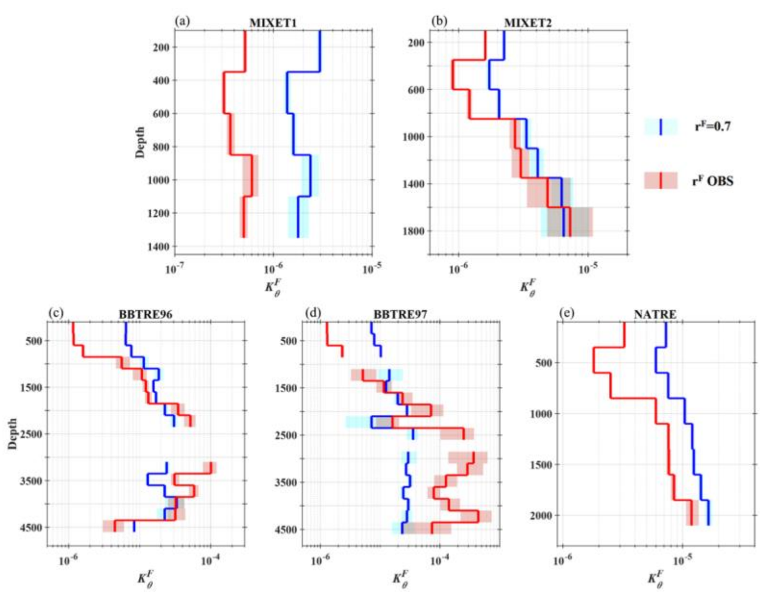

Fig. 14. Vertical profiles of depth-bin mean K_θ^F($K_\theta{}^F{}_c$) based on salt finger patches for the five projects. The blue curves are $K_\theta{}^F{}_c$ estimated with r^F=0.7, and the red ones are K_θ^F based on the measured r^F. The colored shades correspond to 95% bootstrapped confidence intervals. To exclude the influence of extreme values, we only consider patches with ~~Γ^T within~~Γ_θ^F between its upper and lower quartiles for each depth bin. The depth-bin size is 250 m, and depth bins with ~~patch~~ number of patches smaller than 10 are excluded.

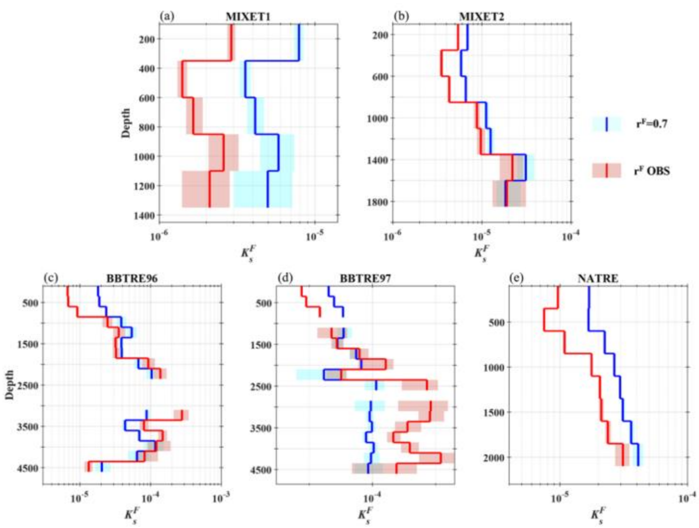

Fig. 15. Same as Fig. 14, but for K_S^F.

Next, we examine vertical variation of the ratio of K_S^F to K_θ^F for the five projects (Fig. 16). For the MIXET1, K_S^F/K_θ^F generally decreases from 5.3 at upper 400 m to 4 at 1400 m, with an averaged value of 4.5. The averaged K_S^F/K_θ^F drops to 3.9 for the MIXET2, and it varies between 3.7 and 4.5 except the small values shallower than 400 m and beneath 1600 m. The BBTRE projects share similar vertical structure of K_S^F/K_θ^F: It has the maximum value of 6 in the upper 800 m, then sharply decreases to 2.5 at 1350 m and keeps at this value until reaching 4600 m. K_S^F/K_θ^F for the NATRE first increases from 3.0 to 4.7 in the upper 800 m, and then sharply decreases to 3 at 1100 m and remains unchanged. From the five projects, K_S^F/K_θ^F generally increases with depth at the upper 1000 m with an average value about 5; then, it sharply drops to around 3 and stays at this value at deeper depths. This ratio is reported to be 2.3 in the western tropical Atlantic (Schmitt et al., 2005), slightly smaller than the result presented here. Van de Boog et al. (2021) presented a global map of K_S^F and K_θ^F based on Argo data and an empirical method; and their results indicate K_S^F/K_θ^F vary between 1.3 and 7.8 for R_ρ ranging from 1 to 4. These earlier works do not show the vertical variation of K_S^F/K_θ^F due to indirect methods used.

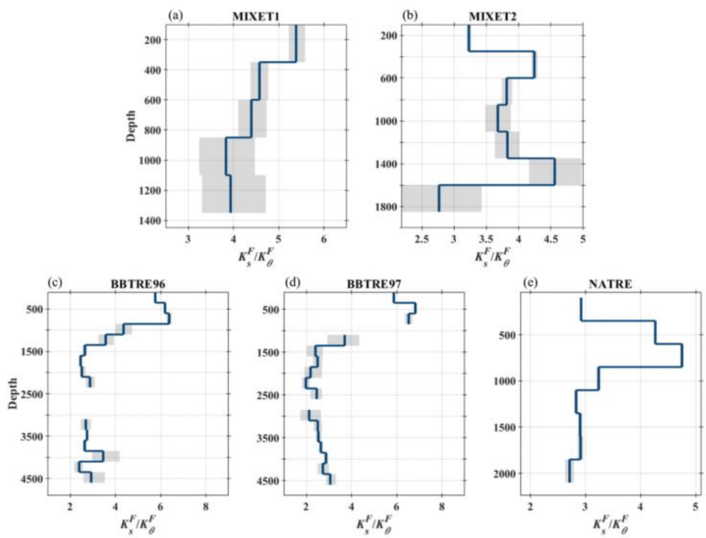

Fig. 16. Vertical profiles of depth-bin mean K_θ^F/K_S^F based on salt finger patches for the five projects. The dark blue curves are the mean K_θ^F/K_S^F, and the gray shadings are 95% bootstrapped confidence intervals. To exclude the influence of extreme values, we only consider patches with ~~Γ^T within~~ Γ_θ^F between its upper and lower quartiles for each depth bin. The depth-bin size is 250 m; and depth bins with ~~patch~~ number of patches smaller than 10 are excluded.

5.3 "Total" eddy diffusivities under superposed salt finger and turbulence

We examine the "total" eddy diffusivities contributed by both salt finger and turbulence by combining the patches with weak turbulence, energetic turbulence and salt finger. Two different methods are used to estimate the "total" eddy diffusivities. The first is from McDougall and Ruddick (1992) (hereinafter MR92). MR92 does not need to differentiate salt finger and turbulent patches; it estimates the total eddy diffusivities by (i) evaluating the departure of observed Γ (Eq. (1)) to a preset reasonable turbulent Γ^T (e.g., Γ^T=0.265) and (ii) introducing a "salt flux enhancement factor", M_0, scaled by R_ρ and r (more details are given in McDougall and Ruddick (1992)). Here, r is treated specifically depending on the mixing type, that is, $r^T=R_\rho$ for turbulence and $r^F=\frac{R_\rho\Gamma}{R_\rho\Gamma+R_\rho-1}$ for salt finger (St. Laurent and Schmitt, 1999). The second is from St. Laurent and Schmitt (1999) (hereinafter LS99), which differentiates turbulence and salt finger firstly, then estimates their eddy diffusivities separately, and finally obtains the total ones as $K_\theta = P^T\cdot K_\theta^T + P^F\cdot K_\theta^F$ and $K_s = P^T\cdot K_s^T + P^F\cdot K_s^F$, where P^T and P^F are the number proportions of turbulence and salt finger patches to their sum, respectively. Fig. 17 shows the "total" K_θ estimated by these two methods. Compared with the BBTREs and NATRE, the results based on MR92 and LS99 present larger differences for MIXETs, which may be due to the fewer patches and more scattered Γ^T and Γ^F. Nonetheless, it is obvious that both estimates have similar magnitude and vertical trend for all the five projects. Comparing the total K_θ with K_θ^T and K_θ^F (Figs. 13, 14), we can see K_θ, especially for the LS99 result, is obviously closer to K_θ^T for all the five projects, confirming that turbulence dominates the observed microstructures. Note that K_θ in the upper 500 m for the BBTREs and NATRE are significantly lower than K_θ^T, seemingly indicating a strong weakening of K_θ due to the prevalence of salt finger. However, the effect of salt finger is actually overestimated, since the dominant hybrid mixing patches at this depth range are all excluded, which should be dominated by turbulence, as indicated by the elevated Re_b. The total K_s is not shown since it is very similar to the situation of K_θ, and the only notable difference is K_s is not significantly weakened by salt finger in the upper 500 m for BBTREs and NATRE, owing to K_s^F is clearly greater than K_θ^F and much closer to K_s^T (Fig. 15).

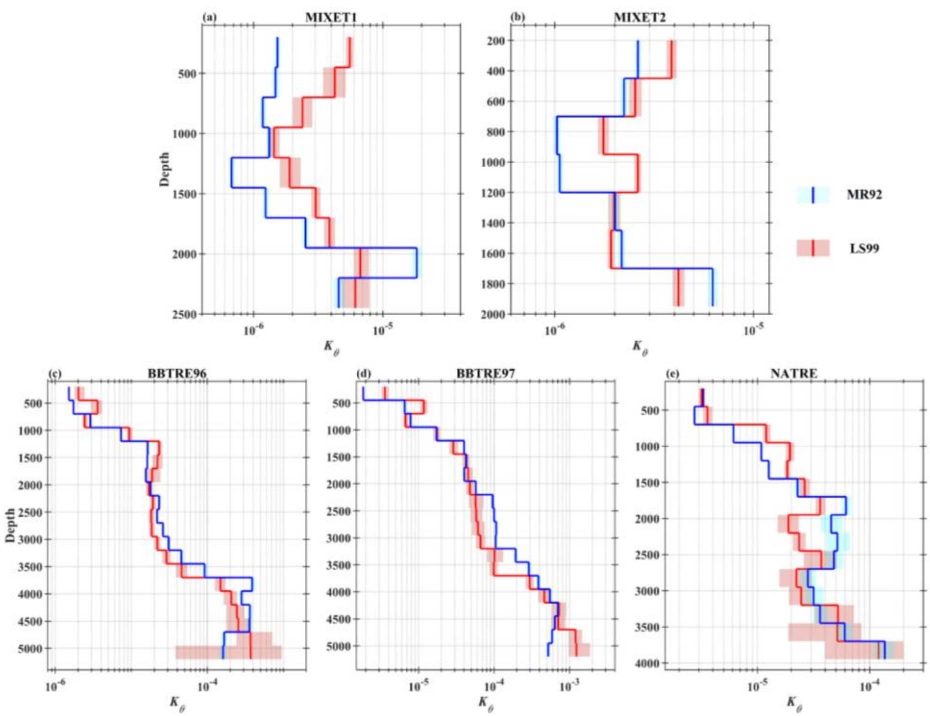

Fig. 17. Vertical profiles of depth-bin averaged total K_θ based on turbulence and salt finger patches for the five projects. The blue curves are results based on MR92, and the red ones are based on LS99. The shades correspond to 95% bootstrapped confidence intervals. The depth-bin size is 250 m, and depth bins with number of patches smaller than 10 are excluded.

6 Summary

The Osborn relation is widely used to estimate vertical eddy diffusivity in practice, assuming a constant dissipation ratio of Γ^{T}=0.2 without identifying underlying mixing mechanisms. The dissipation ratios of heat, salinity and density are equal for turbulent mixing; however, they differ for salt finger-induced mixing. As a result, the eddy diffusivities derived from a constant dissipation ratio would inevitably depart from the actual values. In this study, we differentiated turbulent mixing and salt finger mixing, quantified their dissipation ratios and eddy diffusivities, and examined their relations based on the datasets from "Microstructure Database".

We evaluated the variation of Γ^{T} and its relations with Re_{b} and R_{OT}. The observed Γ^{T} scatters over orders of magnitude, typically from 10^{-2} to 10. The significant difference between the five projects suggests Γ^{T} is highly variable with space and time. ~~Vertically,~~ Γ^{T} in the western equatorial Pacific presents a weak ~~decreasing trend~~decrease downwards, while it increases obviously in the midlatitude in the Atlantic. Although a negative relation between Γ^{T} and Re_{b} was supported by most of the projects, further investigation of the relations of Γ^{T} with Re_{b} and R_{OT} suggested $\Gamma^{T} \propto R_{OT}^{-4/3} \cdot Re_{b}^{1/2}$. This indicates Γ^{T} is modulated by more than one variable, and explains why different relations between Γ^{T} and Re_{b} have been reported (i.e., Mashayek et al., 2017; Ijichi and Hibiya, 2018).

We compared K_{ρ}^{T} estimated using observed Γ^{T} with K_{c} estimated using Γ^{T}=0.2. K_{ρ}^{T} is clearly larger than K_{c}. For the MIXET projects with ~~vertically~~downward weak decreasing Γ^{T}, K_{ρ}^{T} shares similar vertical structure of K_{c}, with magnitude elevated by about two or three times. For the rest projects whose Γ^{T} increases significantly with depth, K_{ρ}^{T} generally presents a much more obvious ~~increasing trend~~increase than K_{c}, and K_{ρ}^{T} can be larger than K_{c} by an order of magnitude. This suggests the intensity of bottom-enhanced mixing may be underestimated when assuming Γ^{T}=0.2.

For salt finger, two "effective" dissipation ratios for heat (Γ_{θ}^{F}) and salt (Γ_{S}^{F}) are derived, and two "artificial" Osborn relations are used to calculate corresponding eddy diffusivities. Γ_{θ}^{F} spans about two orders of magnitude. Both the magnitude and vertical structure of Γ_{θ}^{F} are distinct for the five projects. Γ_{S}^{F} is strongly related to Γ_{θ}^{F}, and they share similar vertical structures, $\Gamma_{S}^{F} \approx 5\Gamma_{\theta}^{F}$. Data from some projects indicate a negative relation between Γ_{θ}^{F} (Γ_{S}^{F}) and Re_{b}, while the others suggest no clear relation. Unlike the existing results indicating r^{F} decreases then asymptotes to a constant value with increasing R_{ρ}, our results suggest r^{F} decreases sharply with R_{ρ} when it is smaller than 2.4 and grows to a larger value with R_{ρ} when it exceeds 2.4.

We examined salt finger-induced K_{θ}^{F} and K_{S}^{F}. Although salt finger becomes rarer with depth, K_{θ}^{F} and K_{S}^{F} increase clearly ~~in the vertical~~with depth, and K_{S}^{F} is greater than K_{θ}^{F}. In the upper 1000 m, K_{S}^{F} is significantly greater than K_{θ}^{F} by about five times for most projects; but below 1000 m, K_{S}^{F}/K_{θ}^{F} generally stays around 3. K_{θ}^{F} and K_{S}^{F} estimated using the observed r^{F} are generally smaller than those using r^{F}=0.7 due to most observed r^{F} being smaller than 0.7, but varying more sharply in the vertical.

Compared with eddy diffusivity induced by turbulence, K_θ^{F} is smaller than K_θ^{T} in the upper 1000 m, but they become more and more comparable with increasing depth. K_S^{F} is close to or even larger than K_S^{T} at all depths for all the projects. In general, although salt finger events are much rare than turbulence at depth (so they ~~may be~~are incapable of largely altering the background mixing intensity shaped by turbulence), they can play a crucial role in local, short-period mixing events, which is worth to be investigated and properly parameterized in numerical models.

Data Availability

The microstructure datasets used in this study are available at http://microstructure.ucsd.edu. And the ETOPO 2022 bathymetry data used in Fig. 1 is from https://www.ncei.noaa.gov/products/etopo-global-relief-model.

Author contributions

The study was conceived and designed by all co-authors. Data preparation, material collection, and analysis were performed by JL. JL prepared the manuscript with contributions from all co-authors.

Competing interests

The contact author has declared that none of the authors has any competing interests.

Acknowledgments

We thank the Climate Process Team for publicly sharing the "Microstructure Database". This work is supported by the National Natural Science Foundation of China (Grants 42076012, 42376012), the Postdoctoral Fellowship Program of CPSF (Grant GZC20241610~~) and~~), the China Postdoctoral Science Foundation (Grant 2024M753046) and the Fundamental Research Funds for the Central Universities (Grant 202413031)).

References

Ashin, K., Girishkumar, M. S., D'Asaro, E., Jofia, J., Sherin, V. R., Sureshkumar, N., and Rao, E. P. R.: Observational evidence of salt finger in the diurnal thermocline, Sci. Rep., 13, 3627, https://doi.org/10.1038/s41598-023-30564-5, 2023.

Barry, M. E., Ivey, G. N., Winters, K. B., and Imberger, J.: Measurements of diapycnal diffusivities in stratified fluids, J. Fluid Mech., 442, 267–291, https://doi.org/10.1017/S0022112001005080, 2001.

van der Boog, C. G., Dijkstra, H. A., Pietrzak, J. D., and Katsman, C. A.: Double-diffusive mixing makes a small contribution to the global ocean circulation, Commun. Earth Environ., 2, 1–9, https://doi.org/10.1038/s43247-021-00113-x, 2021.

Cimoli, L., Caulfield, C. cille P., Johnson, H. L., Marshall, D. P., Mashayek, A., Naveira Garabato, A. C., and Vic, C.: Sensitivity of Deep Ocean Mixing to Local Internal Tide Breaking and Mixing Efficiency, Geophys. Res. Lett., 46, 14622–14633, https://doi.org/10.1029/2019GL085056, 2019.

Dillon, T. M.: Vertical overturns: A comparison of Thorpe and Ozmidov length scales, J. Geophys. Res., 87, 9601–9613, https://doi.org/10.1029/jc087ic12p09601, 1982.

Fine, E. C., MacKinnon, J. A., Alford, M. H., Middleton, L., Taylor, J., Mickett, J. B., Cole, S. T., Couto, N., Boyer, A. L., and Peacock, T.: Double Diffusion, Shear Instabilities, and Heat Impacts of a Pacific Summer Water Intrusion in the Beaufort Sea, J. Phys. Oceanogr., 52, 189–203, https://doi.org/10.1175/JPO-D-21-0074.1, 2022.

Gregg, M. C., Sanford, T. B., and Winkel, D. P.: Reduced mixing from the breaking of internal waves in equatorial waters, Nature, 422, 513–515, https://doi.org/10.1038/nature01507, 2003.

Gregg, M. C., D'Asaro, E. A., Riley, J. J., and Kunze, E.: Mixing efficiency in the ocean, Annu. Rev. Mar. Sci., 10, 443–473, https://doi.org/10.1146/annurev-marine-121916-063643, 2018.

Ijichi, T. and Hibiya, T.: Observed variations in turbulent mixing efficiency in the deep ocean, J. Phys. Oceanogr., 48, 1815–1830, https://doi.org/10.1175/JPO-D-17-0275.1, 2018.

Ijichi, T., St. Laurent, L., Polzin, K. L., and Toole, J. M.: How Variable Is Mixing Efficiency in the Abyss?, Geophys. Res. Lett., 47, e2019GL086813, https://doi.org/10.1029/2019GL086813, 2020.

Inoue, R., Yamazaki, H., Wolk, F., Kono, T., and Yoshida, J.: An Estimation of Buoyancy Flux for a Mixture of Turbulence and Double Diffusion, J. Phys. Oceanogr., 37, 611–624, https://doi.org/10.1175/JPO2996.1, 2007.

Jackson, L., Hallberg, R., and Legg, S.: A Parameterization of Shear-Driven Turbulence for Ocean Climate Models, J. Phys. Oceanogr., 38, 1033–1053, https://doi.org/10.1175/2007JPO3779.1, 2008.

Jackson, P. R. and Rehmann, C. R.: Laboratory Measurements of Differential Diffusion in a Diffusively Stable, Turbulent Flow, J. Phys. Oceanogr., 33, 1592–1603, https://doi.org/10.1175/2405.1, 2003.

Jayne, S. R.: The Impact of Abyssal Mixing Parameterizations in an Ocean General Circulation Model, J. Phys. Oceanogr., 39, 1756–1775, https://doi.org/10.1175/2009JPO4085.1, 2009.

Kelley, D.: Oceanic thermocline staircase, Ph.D. thesis, Dalhousie University, Canada 1986.

Klymak, J. M. and Legg, S. M.: A simple mixing scheme for models that resolve breaking internal waves, Ocean Modell., 33, 224–234, https://doi.org/10.1016/j.ocemod.2010.02.005, 2010.

Kukulka, T., Law, K. L., and Proskurowski, G.: Evidence for the Influence of Surface Heat Fluxes on Turbulent Mixing of Microplastic Marine Debris, J. Phys. Oceanogr., 46, 809–815, https://doi.org/10.1175/JPO-D-15-0242.1, 2016.

Kunze, E.: Limits on growing, finite length salt fingers: a Richardson number constraint. J. Mar. Res., 45, 533–556. 1987.

Li, J., Yang, Q., Sun, H., Zhang, S., Xie, L., Wang, Q., Zhao, W., and Tian, J.: On the Variation of Dissipation Flux Coefficient in the Upper South China Sea, J. Phys. Oceanogr., 53, 551–571, https://doi.org/10.1175/JPO-D-22-0127.1, 2023.

MacKinnon, J. A. and Gregg, M. C.: Mixing on the Late-Summer New England Shelf—Solibores, Shear, and Stratification, J. Phys. Oceanogr., 33, 1476–1492, https://doi.org/10.1175/1520-0485(2003)033<1476:MOTLNE>2.0.CO;2, 2003.

MacKinnon, J. A., Zhao, Z., Whalen, C. B., Waterhouse, A. F., Trossman, D. S., Sun, O. M., Laurent, L. C. S., Simmons, H. L., Polzin, K., Pinkel, R., Pickering, A., Norton, N. J., Nash, J. D., Musgrave, R., Merchant, L. M., Melet, A. V., Mater, B., Legg, S., Large, W. G., Kunze, E., Klymak, J. M., Jochum, M., Jayne, S. R., Hallberg, R. W., Griffies, S. M., Diggs, S., Danabasoglu, G., Chassignet, E. P., Buijsman, M. C., Bryan, F. O., Briegleb, B. P., Barna, A., Arbic, B. K., Ansong, J. K., and Alford, M. H.: Climate Process Team on Internal Wave–Driven Ocean Mixing, Bull. Am. Meteorol. Soc., 98, 2429–2454, https://doi.org/10.1175/BAMS-D-16-0030.1, 2017.

Mashayek, A., Salehipour, H., Bouffard, D., Caulfield, C. P., Ferrari, R., Nikurashin, M., Peltier, W. R., and Smyth, W. D.: Efficiency of turbulent mixing in the abyssal ocean circulation, Geophys. Res. Lett., 44, 6296–6306, https://doi.org/10.1002/2016GL072452, 2017.

Mater, B. D., Venayagamoorthy, S. K., Laurent, L. S., and Moum, J. N.: Biases in thorpe-scale estimates of turbulence dissipation. Part I: Assessments from large-scale overturns in oceanographic data, J. Phys. Oceanogr., 45, 2497–2521, https://doi.org/10.1175/JPO-D-14-0128.1, 2015.

McDougall, T. J.: Some Implications of Ocean Mixing for Ocean Modell., in: Elsevier Oceanography Series, vol. 46, edited by: Nihoul, J. C. J. and Jamart, B. M., Elsevier, 21–35, https://doi.org/10.1016/S0422-9894(08)70535-X, 1988.

McDougall, T. J. and Ruddick, B. R.: The use of ocean microstructure to quantify both turbulent mixing and salt-fingering, Deep. Sea Res. Part A Oceanogr. Res. Pap., 39, 1931–1952, https://doi.org/10.1016/0198-0149(92)90006-F, 1992.

Monismith, S. G., Koseff, J. R., and White, B. L.: Mixing Efficiency in the Presence of Stratification: When Is It Constant?, Geophys. Res. Lett., 45, 5627–5634, https://doi.org/10.1029/2018GL077229, 2018.

Moum, J. N.: Efficiency of mixing in the main thermocline, J. Geophys. Res., 101, 12057–12069, https://doi.org/10.1029/96JC00508, 1996.

Nagai, T., Inoue, R., Tandon, A., and Yamazaki, H.: Evidence of enhanced double-diffusive convection below the main stream of the Kuroshio Extension, J. Geophys. Res., 120, 8402–8421, https://doi.org/10.1002/2015JC011288, 2015.

Oakey, N. S.: Statistics of Mixing Parameters in the Upper Ocean During JASIN Phase 2, J. Phys. Oceanogr., 15, 1662–1675, https://doi.org/10.1175/1520-0485(1985)015<1662:SOMPIT>2.0.CO;2, 1985.

Osborn, T. R.: Estimates of the Local Rate of Vertical Diffusion from Dissipation Measurements, J. Phys. Oceanogr., 10, 83–89, https://doi.org/10.1175/1520-0485(1980)010<0083:EOTLRO>2.0.CO;2, 1980.

Osborn, T. R. and Cox, C. S.: Oceanic fine structure, Geophys. Fluid Dyn., 3, 321–345, https://doi.org/10.1080/03091927208236085, 1972.

Oyabu, R., Yasuda, I., and Sasaki, Y.: Large-Scale Distribution and Variations of Active Salt-Finger Double-Diffusion in the Western North Pacific, J. Phys. Oceanogr., 53, 2013–2027, https://doi.org/10.1175/JPO-D-22-0244.1, 2023.

Polzin, K. and Ferrari, R.: Isopycnal Dispersion in NATRE, J. Phys. Oceanogr., 34, 247–257, https://doi.org/10.1175/1520-0485(2004)034<0247:IDIN>2.0.CO;2, 2004.

Polzin, K. L., Toole, J. M., Ledwell, J. R., and Schmitt, R. W.: Spatial Variability of Turbulent Mixing in the Abyssal Ocean, Science, 276, 93–96, https://doi.org/10.1126/science.276.5309.93, 1997.

Pujiana, K., Moum, J. N., and Smyth, W. D.: The Role of Turbulence in Redistributing Upper-Ocean Heat, Freshwater, and Momentum in Response to the MJO in the Equatorial Indian Ocean, J. Phys. Oceanogr., 48, 197–220, https://doi.org/10.1175/JPO-D-17-0146.1, 2018.

Radko, T. and Smith, D. P.: Equilibrium transport in double-diffusive convection, J. Fluid Mech., 692, 5–27, https://doi.org/10.1017/jfm.2011.343, 2012.

Richards, K. J., Natarov, A., Firing, E., Kashino, Y., Soares, S. M., Ishizu, M., Carter, G. S., Lee, J. H., and Chang, K. I.: Shear-generated turbulence in the equatorial Pacific produced by small vertical scale flow features, J. Geophys. Res., 120, 3777–3791, https://doi.org/10.1002/2014JC010673, 2015.

Ruddick, B.: A practical indicator of the stability of the water column to double-diffusive activity, *Deep-Sea Res.*, 30, 1105–1107, https://doi.org/10.1016/0198-0149(83)90063-8, 1983.

Sabine, C. L., Feely, R. A., Gruber, N., Key, R. M., Lee, K., Bullister, J. L., Wanninkhof, R., Wong, C. S., Wallace, D. W. R., Tilbrook, B., Millero, F. J., Peng, T.-H., Kozyr, A., Ono, T., and Rios, A. F.: The Oceanic Sink for Anthropogenic CO2, Science, 305, 367–371, https://doi.org/10.1126/science.1097403, 2004.

Salehipour, H., Caulfield, C. P., and Peltier, W. R.: Turbulent mixing due to the Holmboe wave instability at high Reynolds number, J. Fluid Mech., 803, 591–621, https://doi.org/10.1017/jfm.2016.488, 2016.

Schmitt, R. W.: Double Diffusion in Oceanography, Annu. Rev. Fluid Mech., 26, 255–285, https://doi.org/10.1146/annurev.fl.26.010194.001351, 1994.

Schmitt, R. W., Ledwell, J. R., Montgomery, E. T., Polzin, K. L., and Toole, J. M.: Enhanced Diapycnal Mixing by Salt Fingers in the Thermocline of the Tropical Atlantic, Science, 308, 685–688, https://doi.org/10.1126/science.1108678, 2005.

Shih, L. H., Koseff, J. R., Ivey, G. N., and Ferziger, J. H.: Parameterization of turbulent fluxes and scales using homogeneous sheared stably stratified turbulence simulations, J. Fluid Mech., 525, 193–214, https://doi.org/10.1017/S0022112004002587, 2005.

Smyth, W. D., Moum, J. N., and Caldwell, D. R.: The efficiency of mixing in turbulent patches: Inferences from direct simulations and microstructure observations, J. Phys. Oceanogr., 31, 1969–1992, https://doi.org/10.1175/1520-0485(2001)031<1969:teomit>2.0.co;2, 2001.

St. Laurent, L. and Schmitt, R. W.: The contribution of salt fingers to vertical mixing in the North Atlantic Tracer Release Experiment, J. Phys. Oceanogr., 29, 1404–1424, https://doi.org/10.1175/1520-0485(1999)029<1404:tcosft>2.0.co;2, 1999.

St. Laurent, L., Garabato, A. C. N., Ledwell, J. R., Thurnherr, A. M., Toole, J. M., and Watson, A. J.: Turbulence and Diapycnal Mixing in Drake Passage, J. Phys. Oceanogr., 42, 2143–2152, https://doi.org/10.1175/JPO-D-12-027.1, 2012.

Vladoiu, A., Bouruet-Aubertot, P., Cuypers, Y., Ferron, B., Schroeder, K., Borghini, M., and Leizour, S.: Contrasted mixing efficiency in energetic versus quiescent regions: Insights from microstructure measurements in the Western Mediterranean Sea, Prog. Oceanogr., 195, 102594, https://doi.org/10.1016/j.pocean.2021.102594, 2021.

Waterhouse, A. F., MacKinnon, J. A., Nash, J. D., Alford, M. H., Kunze, E., Simmons, H. L., Polzin, K. L., Laurent, L. C. S., Sun, O. M., Pinkel, R., Talley, L. D., Whalen, C. B., Huussen, T. N., Carter, G. S., Fer, I., Waterman, S., Garabato, A. C. N., Sanford, T. B., and Lee, C. M.: Global Patterns of Diapycnal Mixing from Measurements of the Turbulent Dissipation Rate, J. Phys. Oceanogr., 44, 1854–1872, https://doi.org/10.1175/JPO-D-13-0104.1, 2014.

Whitt, D. B., Lévy, M., and Taylor, J. R.: Low-frequency and high-frequency oscillatory winds synergistically enhance nutrient entrainment and phytoplankton at fronts, J. Geophys. Res., 122, 1016–1041, https://doi.org/10.1002/2016JC012400, 2017.

Wunsch, C. and Ferrari, R.: Vertical mixing, energy, and the general circulation of the oceans, Annu. Rev. Fluid Mech., 36, 281–314, https://doi.org/10.1146/annurev.fluid.36.050802.122121, 2004.